

See discussions, stats, and author profiles for this publication at: <https://www.researchgate.net/publication/225285940>

# Ligand K-Edge and Metal L-Edge X-ray Absorption Spectroscopy and Density Functional Calculations of Oxomolybdenum Complexes with Thiolate and Related Ligands: Implications for Sulf...

ARTICLE *in* JOURNAL OF THE AMERICAN CHEMICAL SOCIETY · NOVEMBER 1999

Impact Factor: 12.11 · DOI: 10.1021/ja9903678

---

CITATIONS

54

---

READS

7

9 AUTHORS, INCLUDING:



Yasuo Izumi

Chiba University

124 PUBLICATIONS 1,186 CITATIONS

SEE PROFILE



Partha Basu

Duquesne University

101 PUBLICATIONS 2,518 CITATIONS

SEE PROFILE

# Ligand K-Edge and Metal L-Edge X-ray Absorption Spectroscopy and Density Functional Calculations of Oxomolybdenum Complexes with Thiolate and Related Ligands: Implications for Sulfite Oxidase

Yasuo Izumi,<sup>†,§</sup> Thorsten Glaser,<sup>†</sup> Kendra Rose,<sup>†</sup> Jonathan McMaster,<sup>⊥</sup> Partha Basu,<sup>⊥</sup> John H. Enemark,<sup>\*,⊥</sup> Britt Hedman,<sup>\*,†,‡</sup> Keith O. Hodgson,<sup>\*,†,‡</sup> and Edward I. Solomon<sup>\*,†</sup>

Contribution from the Department of Chemistry and Stanford Synchrotron Radiation Laboratory, Stanford University, Stanford, California 94305, and Department of Chemistry, University of Arizona, Tucson, Arizona 85721

Received February 5, 1999

**Abstract:** X-ray absorption spectra have been measured at the S K-, Cl K-, and Mo L<sub>3</sub>- and L<sub>2</sub>-edges for the d<sup>0</sup> dioxomolybdenum(VI) complexes LMoO<sub>2</sub>(SCH<sub>2</sub>Ph), LMoO<sub>2</sub>Cl, and LMoO<sub>2</sub>(OPh) (L = hydrotris(3,5-dimethyl-1-pyrazolyl)borate) to investigate ligand–metal covalency and its effects on oxo transfer reactivity. Two dominant peaks are observed at the S K-edge (2470.5 and 2472.5 eV) for LMoO<sub>2</sub>(SCH<sub>2</sub>Ph) and at the Cl K-edge (2821.9 and 2824.2 eV) for LMoO<sub>2</sub>Cl, demonstrating two major covalent contributions from S and Cl to the Mo d orbitals. Density functional calculations were performed on models of the three Mo complexes, and the energies and characters of the Mo 4d orbitals were interpreted in terms of the effects of two strong *cis*-oxo bonds and additional perturbations due to the thiolate, chloride, or alkoxide ligand. The major perturbation effects are for thiolate and Cl<sup>−</sup>  $\pi$  mixed with the d<sub>xz</sub> orbital and  $\sigma$  mixed with the d<sub>z<sup>2</sup></sub> orbital. The calculated 4d orbital energy splittings for models of these two major contributions to the bonding of thiolate and Cl ligands (2.47 and 2.71 eV, respectively) correspond to the splittings observed experimentally for the two dominant ligand K-edge peaks for LMoO<sub>2</sub>(SCH<sub>2</sub>Ph) and LMoO<sub>2</sub>Cl (2.0 and 2.3 eV, respectively) after consideration of final state electronic relaxation. Quantification of the S and Cl covalencies in the d orbital manifold from the pre-edge intensity yields, ~42% and ~17% for LMoO<sub>2</sub>(SCH<sub>2</sub>Ph) and LMoO<sub>2</sub>Cl, respectively. The Mo L<sub>2</sub>-edge spectra provide a direct probe of metal 4d character for the three Mo complexes. The spectra contain a strong, broad peak and two additional sharp peaks at higher energy, which are assigned to 2p transitions to the overlapping t<sub>2g</sub> set and to the d<sub>z<sup>2</sup></sub> and d<sub>xy</sub> levels, respectively. The total peak intensities of the Mo L<sub>2</sub>-edges for LMoO<sub>2</sub>(OPh) and LMoO<sub>2</sub>Cl are similar to and larger than those for LMoO<sub>2</sub>(SCH<sub>2</sub>Ph), which agrees with the calculated trend in ligand–metal covalency. The theoretical and experimental description of bonding developed from these studies provides insight into the relationship of electronic structure to the oxo transfer chemistry observed for the LMoO<sub>2</sub>X complexes. These results imply that anisotropic covalency of the Mo–S<sub>cys</sub> bond in sulfite oxidase may promote preferential transfer of one of the oxo groups during catalysis.

## 1. Introduction

Mo-containing enzymes are essential for all forms of life. With the exception of nitrogenase, most of these enzymes catalyze reactions in which there is a net transfer of an oxygen atom between substrate and water, as shown in eq 1.<sup>1</sup>



Prior to 1995, structural information about the Mo centers in these enzymes was deduced principally from EXAFS at the Mo K-edge and EPR spectroscopy of their transient Mo(V) states.<sup>1</sup> Since then, several protein crystal structures have been reported.<sup>2–11</sup> These protein structures confirm that there are three distinct structural families for the Mo centers: the xanthine oxidase, DMSO reductase, and sulfite oxidase families.<sup>1</sup> In all

three structural families, the Mo center is coordinated by S donors from the *cis*-ene-1,2-dithiolate (dithiolene) of one (or two) novel pyranopterin (molybdopterin) units.<sup>1,12</sup> This ligand system is unique to Mo and W in metalloproteins, and it appears that coordination by this ligand (and in some cases an additional S ligand) is essential for the catalytic function of these enzymes.

(2) Romão, M. J.; Archer, M.; Moura, I.; Moura, J. J. G.; LeGall, J.; Engh, R.; Schneider, M.; Hof, P.; Huber, R. *Science* **1995**, 270, 1170–1176.

(3) Huber, R.; Hof, P.; Dauter, R. O.; Moura, J. J. G.; Moura, I.; Liu, M. Y.; Legall, J.; Hille, R.; Archer, M.; Romão, M. *Proc. Natl. Acad. Sci. U.S.A.* **1996**, 93, 8846–8851.

(4) Schindelin, H.; Kisker, C.; Hilton, J.; Rajagopalan, K. V.; Rees, D. C. *Science* **1996**, 272, 1615–1621.

(5) Schneider, F.; Löwe, J.; Huber, R.; Schindelin, H.; Kisker, C.; Knäblein, J. *J. Mol. Biol.* **1996**, 263, 53–59.

(6) McAlpine, A. S.; McEwan, A. G.; Shaw, A. L.; Bailey, S. *J. Biol. Inorg. Chem.* **1997**, 2, 690–701.

(7) McAlpine, A. S.; McEwan, A. G.; Bailey, S. *J. Mol. Biol.* **1998**, 275, 613–623.

(8) Boyington, J. C.; Gladyshev, V. N.; Khangulov, S. V.; Stadtman, T. C.; Sun, P. D. *Science* **1997**, 275, 1305–1308.

(9) Kisker, C.; Schindelin, H.; Pacheco, A.; Wehbi, W. A.; Garrett, R. M.; Rajagopalan, K. V.; Enemark, J. H.; Rees, D. C. *Cell* **1997**, 91, 973–983.

\* To whom correspondence should be addressed.

<sup>†</sup> Stanford University.

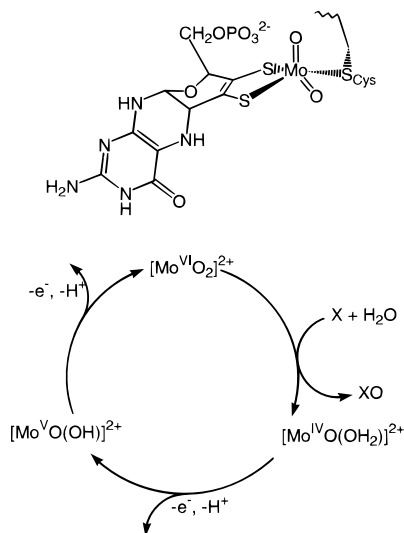
<sup>‡</sup> Stanford Synchrotron Radiation Laboratory, SLAC.

<sup>⊥</sup> The University of Arizona.

<sup>§</sup> On leave from Interdisciplinary Graduate School of Science and Engineering, Tokyo Institute of Technology, Yokohama, Japan.

(1) Hille, R. *Chem. Rev.* **1996**, 96, 2757–2816.

**Scheme 1.** (Top) Coordination of the Mo Site of Sulfite Oxidase, Showing the Novel Pyranopterin That Contributes the Ene-1,2-dithiolate Group, and (Bottom) Proposed Reaction Cycle for Sulfite Oxidase<sup>a</sup>



<sup>a</sup> Sulfite (X) is oxidized by oxygen atom transfer (OAT) from  $[\text{Mo}^{\text{VI}}\text{O}_2]^{2+}$ , water coordinates to the reduced  $[\text{Mo}^{\text{IV}}\text{O}(\text{H}_2\text{O})]^{2+}$  center, and two successive coupled electron–proton transfers reoxidize the Mo site back to  $[\text{Mo}^{\text{VI}}\text{O}_2]^{2+}$ .

The coordination about the Mo atom from the X-ray crystal structure of chicken liver sulfite oxidase at 1.9 Å resolution is shown in Scheme 1.<sup>9</sup> The Mo atom is five-coordinate and exhibits approximate square pyramidal coordination geometry, with oxygen atoms in the axial and equatorial positions. Both EXAFS<sup>13–16</sup> and resonance Raman spectroscopy<sup>17</sup> indicate that the oxidized enzyme possesses two oxo groups coordinated to a Mo(VI) center. The remaining equatorial positions are occupied by the two S atoms from one ene-1,2-dithiolate ligand and the S atom from the side chain of a cysteine that is conserved throughout all sulfite oxidases. Site-directed mutagenesis of this cysteine to serine in the human or rat enzymes results in an inactive enzyme.<sup>18</sup>

The proposed reaction cycle for the Mo center of sulfite oxidase (Scheme 1) involves the transfer of an O atom from a dioxo-Mo(VI) center of the enzyme to sulfite to generate an oxo-Mo(IV) center and sulfate.<sup>19</sup> The active site is regenerated by two consecutive one-electron processes involving the heme prosthetic groups in the protein and ultimately cytochrome *c*. The first electron-transfer reaction generates a paramagnetic Mo(V) state that can be detected by EPR spectroscopy.<sup>15,20–23</sup>

Single turnover experiments on DMSO reductase from *Rhodobacter sphaeroides*<sup>24</sup> and on xanthine oxidase<sup>25</sup> are consistent with oxygen atom transfer (OAT) at the Mo center in these enzymes and provide support for Scheme 1, proposed for sulfite oxidase.

Extensive investigations into the chemistry of oxomolybdenum(IV), -(V), and -(VI) have accompanied the studies on the native sulfite oxidases.<sup>19,26–28</sup> Analogues incorporating the facially coordinating hydrotris(3,5-dimethyl-1-pyrazolyl)borate (L) ligand have been particularly successful as functional mimics for enzymes with  $[\text{Mo}^{\text{VI}}\text{O}_2]^{2+}$  centers. The reaction of  $\text{LMo}^{\text{VI}}\text{O}_2\text{X}$  (X = Cl, Br, OPh, SPh,  $\text{SCH}_2\text{Ph}$ ,  $\text{SCH}(\text{CH}_3)_2$ ) with  $\text{PPh}_3$  generates an unsaturated “ $\text{LMo}^{\text{IV}}\text{OX}$ ” center that can be trapped with pyridine to form  $\text{LMo}^{\text{IV}}\text{OX}(\text{pyridine})$ . In wet, oxygenated solvents, “ $\text{LMo}^{\text{IV}}\text{OX}$ ” undergoes two successive one-electron reactions through a paramagnetic  $\text{LMo}^{\text{VOX}}(\text{OH})$  intermediate to regenerate the catalytic  $\text{LMo}^{\text{VI}}\text{O}_2\text{X}$  complex.<sup>29–31</sup> Isotopic oxygen atom tracer studies on this system demonstrate that the O atom transferred to  $\text{PPh}_3$  derives from the  $[\text{MoO}_2]^{2+}$  center and that  $\text{H}_2\text{O}$ , not dioxygen, is the ultimate source of the O atoms.<sup>32</sup> This is the only synthetic system that incorporates the key features of Scheme 1, proposed for the catalytic cycle of sulfite oxidase. A theoretical study on the energetics of this catalytic cycle reveals that the direction of approach of the substrate to the  $[\text{Mo}^{\text{VI}}\text{O}_2]^{2+}$  center in the OAT step is critical to maximizing the stability of the “ $\text{LMo}^{\text{IV}}\text{OX}(\text{OPPh}_3)$ ” adduct.<sup>33</sup> The calculations also indicate that the displacement of the oxidized substrate from the “ $\text{LMo}^{\text{IV}}\text{OX}(\text{OPPh}_3)$ ” center by  $\text{H}_2\text{O}$  occurs through a concerted associative mechanism. The Mo(IV), Mo(V), and Mo(VI) intermediates in the catalytic cycle have been trapped and examined structurally and spectroscopically.<sup>29–32</sup>  $\text{LMo}^{\text{VOY}}_2$  (Y = SR, OR; R = alkyl, aryl) have been subjected to extensive EPR, PES (photoelectron spectroscopy), and MCD (magnetic circular dichroism) studies, and an electronic structure model for these complexes has been developed.<sup>34–37</sup> These studies reveal considerable S ligand contribution to the singly occupied  $d_{xy}$  orbital of these complexes. The relative rates of OAT catalysis by  $\text{LMo}^{\text{VI}}\text{O}_2\text{X}$  depend on X (X = Cl > SR > OR) (Table 1).<sup>30,32</sup>

(10) Czjzek, M.; Dos Santos, J.-P.; Pommier, J.; Giordano, G.; Méjean, V.; Haser, R. *J. Mol. Biol.* **1998**, *284*, 435–437.

(11) Dias, J. M.; Than, M. E.; Humm, A.; Huber, R.; Bourenkov, G. P.; Bartunik, H. D.; Bursakov, S.; Calvete, J.; Caldeira, J.; Carneiro, C.; Moura, J. J. G.; Moura, I.; Romão, M. J. *Structure* **1999**, *7*, 65–79.

(12) Rajagopalan, K. V. *Adv. Enzymol. Relat. Areas Mol. Biol.* **1991**, *64*, 215–289.

(13) Cramer, S. P.; Wahl, R.; Rajagopalan, K. V. *J. Am. Chem. Soc.* **1981**, *103*, 7721–7727.

(14) George, G. N.; Garrett, R. M.; Prince, R. C.; Rajagopalan, K. V. *J. Am. Chem. Soc.* **1996**, *118*, 8588–8592.

(15) George, G. N.; Kipke, C. A.; Prince, R. C.; Sunde, R. A.; Enemark, J. H.; Cramer, S. P. *Biochemistry* **1989**, *28*, 5075–5080.

(16) George, G. N.; Pickering, I. J.; Kisker, C. *Inorg. Chem.* **1999**, *38*, 2539–2540.

(17) Garton, S. D.; Garrett, R. M.; Rajagopalan, K. V.; Johnson, M. K. *J. Am. Chem. Soc.* **1997**, *119*, 2590–2591.

(18) Garrett, R. M.; Rajagopalan, K. V. *J. Biol. Chem.* **1996**, *271*, 7387–7391.

(19) Enemark, J. H.; Young, C. G. *Adv. Inorg. Chem.* **1993**, *40*, 1–88.

(20) Lamy, M. T.; Gutteridge, S.; Bray, R. C. *Biochem. J.* **1980**, *185*, 397–403.

(21) Bray, R. C.; Gutteridge, S.; Lamy, M. T.; Wilkinson, T. *Biochem. J.* **1983**, *211*, 227–236.

(22) George, G. N.; Prince, R. C.; Kipke, C. A.; Sunde, R. A.; Enemark, J. H. *Biochem. J.* **1988**, *256*, 307–309.

(23) Gutteridge, S.; Lamy, M. T.; Bray, R. C. *Biochem. J.* **1980**, *191*, 285–288.

(24) Schultz, B. E.; Hille, R.; Holm, R. H. *J. Am. Chem. Soc.* **1995**, *117*, 827–828.

(25) Hille, R.; Sprecher, H. *J. Biol. Chem.* **1987**, *262*, 10914–10917.

(26) Holm, R. H. *Chem. Rev.* **1987**, *87*, 1401–1449.

(27) Holm, R. H. *Coord. Chem. Rev.* **1990**, *100*, 183–221.

(28) Schultz, B. E.; Holm, R. H. *Inorg. Chem.* **1993**, *32*, 4244–4248.

(29) Xiao, Z.; Bruck, M. A.; Doyle, C.; Enemark, J. H.; Grittini, C.; Gable, R. W.; Wedd, A. G.; Young, C. G. *Inorg. Chem.* **1995**, *34*, 5950–5962.

(30) Roberts, S. A.; Young, C. G.; Kipke, C. A.; Cleland, W. E.; Yamanouchi, K.; Carducci, M. D.; Enemark, J. H. *Inorg. Chem.* **1990**, *29*, 3650–3656.

(31) Xiao, Z.; Young, C. G.; Enemark, J. H.; Wedd, A. G. *J. Am. Chem. Soc.* **1992**, *114*, 9194–9195.

(32) Xiao, Z.; Bruck, M. A.; Enemark, J. H.; Young, C. G.; Wedd, A. G. *Inorg. Chem.* **1996**, *35*, 7508–7515.

(33) Pietsch, M. A.; Hall, M. B. *Inorg. Chem.* **1996**, *35*, 1273–1278.

(34) Dhawan, I. K.; Enemark, J. H. *Inorg. Chem.* **1996**, *35*, 4873–4882.

(35) Carducci, M. D.; Brown, C.; Solomon, E. I.; Enemark, J. H. *J. Am. Chem. Soc.* **1994**, *116*, 11856–11868.

(36) Holm, R. H.; Berg, J. M. *Acc. Chem. Res.* **1986**, *19*, 363–370.

(37) Inscore, F. E.; McNaughton, R.; Westcott, B. L.; Helton, M. E.; Jones, R.; Dhawan, I. K.; Enemark, J. H.; Kirk, M. L. *Inorg. Chem.* **1999**, *38*, 1401–1410.

**Table 1.** Rate Constants for Reaction of Oxomolybdenum Complexes with PPh<sub>3</sub> at 298 K and Reduction Potentials versus SCE

| complex                                 | $k$ (M <sup>-1</sup> s <sup>-1</sup> )      | $E_{1/2}$ (V) <sup>b</sup> |
|---|---|----------------------------|
| LMoO <sub>2</sub> Cl                    | very fast ( $\geq 10^{-2}$ ) <sup>a,c</sup> | -0.62                      |
| LMoO <sub>2</sub> (SPh)                 | $6 \times 10^{-4}$ <sup>a</sup>             | -0.76                      |
| LMoO <sub>2</sub> (SCH <sub>2</sub> Ph) |   | -0.84                      |
| LMoO <sub>2</sub> (OPh)                 | $2 \times 10^{-6}$ <sup>a</sup>             | -0.88                      |
| LMoO <sub>2</sub> (OCH <sub>3</sub> )   | $\sim 0$ <sup>a</sup>                       | -1.13                      |

<sup>a</sup> Reference 30. <sup>b</sup> Reference 29. <sup>c</sup> Reaction was too fast to be quantitatively measured.

The analysis of pre-edge X-ray absorption spectra (XAS) is established as an effective probe of the electronic structure of an absorbing atom. Metal K-edge<sup>38–43</sup> and L-edge<sup>44–47</sup> XAS provides a direct measure of the metal contribution to the half or unoccupied valence antibonding molecular orbitals. Ligand K-edge XAS<sup>48–59</sup> provides an experimental estimate of ligand character in these valence orbitals due to covalent bonding, which is similar to information obtained from an analysis of the ligand superhyperfine splittings obtained from EPR. How-

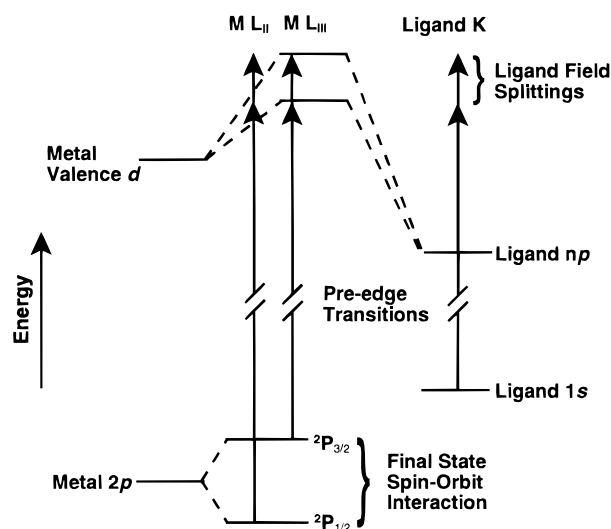


**Figure 1.** Schematic representation of the contributions to the energy of the ligand K-edge and metal L-edge pre-edge features. The ligand K-edge observes the transition from the ligand 1s to the antibonding orbital(s) of metal *md* with ligand *np*. Metal L<sub>3</sub>- and L<sub>2</sub>-edges are the transitions from  $2p_{3/2}$  and  $2p_{1/2}$  terms, respectively, to metal *md*, split by the spin-orbit interaction due to the final state spin-orbit coupling.

(38) Heald, S. M.; Tranquanda, J. M. In *Physical Methods of Chemistry*; Rossiter, B. W., Hamilton, J. F., Eds.; Wiley: New York, 1990; Vol. 5, pp 189–272.

(39) Bianconi, A. In *X-ray Absorption*; Koningsbeiger, D. C., Prins, R., Eds.; Wiley: New York, 1988; pp 573–662.

(40) Kau, L. S.; Spira-Solomon, D. J.; Penner-Hahn, J. E.; Hodgson, K. O.; Solomon, E. I. *J. Am. Chem. Soc.* **1987**, *109*, 6433–6442.

(41) Roe, A. L.; Schneider, D. J.; Mayer, R. J.; Pyrz, J. W.; Widom, J.; Que, L., Jr. *J. Am. Chem. Soc.* **1984**, *106*, 1676–1681.

(42) Eidsness, M. K.; Sullivan, R. J.; Scott, R. A. In *Bioinorganic Chemistry of Nickel*; Lancaster, J. R., Ed.; VCH: Deerfield Beach, FL, 1988; pp 73–92.

(43) Conradson, S. D.; Burgess, B. K.; Newton, W. E.; McDonald, J. W.; Robinson, J. R.; Gheller, S. F.; Mortenson, L. W.; Adams, M. W. W.; Mascharack, P. K.; Armstrong, W. A.; Holm, R. H.; Hodgson, K. O. *J. Am. Chem. Soc.* **1985**, *107*, 7935–7940.

(44) George, S. J.; Lowery, M. D.; Solomon, E. I.; Cramer, S. P. *J. Am. Chem. Soc.* **1993**, *115*, 2968–2969.

(45) George, G. N.; Cleland, W. E., Jr.; Enemark, J. H.; Smith, B. E.; Kipke, C. A.; Roberts, S. A.; Cramer, S. P. *J. Am. Chem. Soc.* **1990**, *112*, 2541–2548.

(46) Mansour, A. N.; Cook, J. J.; Sayers, D. E. *J. Phys. Chem.* **1984**, *88*, 2330–2334.

(47) Wang, H.; Ge, P.; Riordan, C. G.; Brooker, S.; Woerner, C. G.; Collins, T.; Melendres, C. A.; Graudejus, O.; Bartlett, N.; Cramer, S. P. *J. Phys. Chem. B* **1998**, *102*, 8343–8346.

(48) Hedman, B.; Hodgson, K. O.; Solomon, E. I. *J. Am. Chem. Soc.* **1990**, *112*, 1643–1645.

(49) Hedman, B.; Frank, P.; Gheller, S. F.; Roe, A. L.; Newton, W. E.; Hodgson, K. O. *J. Am. Chem. Soc.* **1988**, *110*, 3798–3805.

(50) Shadle, S. E.; Penner-Hahn, J. E.; Schugar, H. J.; Hedman, B.; Hodgson, K. O.; Solomon, E. I. *J. Am. Chem. Soc.* **1993**, *115*, 767–776.

(51) Shadle, S. E.; Hedman, B.; Hodgson, K. O.; Solomon, E. I. *Inorg. Chem.* **1994**, *33*, 4235–4244.

(52) (a) Shadle, S. E.; Hedman, B.; Hodgson, K. O.; Solomon, E. I. *J. Am. Chem. Soc.* **1995**, *117*, 2259–2272. (b) Note that the  $R^2$  term in Table 6 of ref 52a is not appropriate for a core-to-valence CT transition: Neese, F.; Hedman, B.; Hodgson, K.; Solomon, E. I. *Inorg. Chem.*, in press.

(53) Rose Williams, K.; Gamelin, D. R.; LaCroix, L. B.; Houser, R. P.; Tolman, W. B.; Mulder, T. C.; de Vries, S.; Hedman, B.; Hodgson, K. O.; Solomon, E. I. *J. Am. Chem. Soc.* **1997**, *119*, 613–614.

(54) Rose Williams, K.; Hedman, B.; Hodgson, K. O.; Solomon, E. I. *Inorg. Chim. Acta* **1997**, *263*, 315–321.

(55) Rempel, A.; Andrews, J. C.; Cinco, R. M.; Wemple, M. W.; Christou, G.; Law, N. A.; Pecoraro, V. L.; Sauer, K.; Yachandra, V. K.; Klein, M. P. *J. Am. Chem. Soc.* **1997**, *119*, 4465–4470.

(56) Rose, K.; Shadle, S. E.; Eidsness, M. K.; Kurtz, D. M., Jr.; Scott, R. A.; Hedman, B.; Hodgson, K. O.; Solomon, E. I. *J. Am. Chem. Soc.* **1998**, *120*, 10743–10747.

(57) Jollet, F.; Petit, T.; Gota, S.; Thromat, N.; Gautiersoyer, M.; Pasturel, A. *J. Phys. Condens. Matter* **1997**, *43*, 9393–9401.

(58) Wu, Z. Y.; Gota, S.; Jollet, F.; Pollak, M.; Gautiersoyer, M.; Natoli, C. R. *Phys. Rev. B* **1997**, *55*, 2570–2577.

(59) Rose, K.; Shadle, S. E.; Glaser, T.; de Vries, S.; Cherepanov, A.; Canters, G. W.; Hedman, B.; Hodgson, K. O.; Solomon, E. I. *J. Am. Chem. Soc.* **1999**, *121*, 2353–2363.

ever, ligand K-edge XAS has the advantage of being applicable to complexes without an EPR signal and to ligands without a nuclear spin.

Ligand K-edge XAS probes the electronic transition from a ligand 1s orbital (Figure 1). The pre-edge feature involves the transition to the antibonding molecular orbital  $\Psi^* = (1 - \alpha'^2)^{1/2}\psi_M - \alpha'\psi_L$ , where  $\psi_M$  and  $\psi_L$  are metal and ligand wave functions, respectively, and  $\alpha'$  is the ligand coefficient in the antibonding molecular orbital  $\Psi^*$ .<sup>48,50–52</sup> The transition intensity of the pre-edge feature is proportional to that of the dipole-allowed ligand-based 1s  $\rightarrow$  3p transition, weighted by its antibonding character in  $\Psi^*$  ( $\alpha'^2$ , eq 2).

$$I(\text{ligand } 1s \rightarrow \Psi^*) = \alpha'^2 I(\text{ligand } 1s \rightarrow 3p) \quad (2)$$

Thus, the pre-edge intensity provides a direct probe of the ligand (S or Cl) covalency in the unoccupied metal d orbitals. The pre-edge energy of the ligand K-edge is dependent on the relative orbital energies of the Mo 4d and ligand 1s levels. These vary with the effective nuclear charges and the ligand field splittings (Figure 1) within the complex.

Metal L-edge spectroscopy probes the electronic transition from the metal 2p orbital to  $\Psi^*$ . Spin-orbit coupling splits the Mo 2p into the  $2p_{3/2}$  (L<sub>3</sub>-edge) and the  $2p_{1/2}$  (L<sub>2</sub>-edge) states, separated by  $\sim 105$  eV (Figure 1). The intensity of these transitions is proportional to the dipole-allowed 2p  $\rightarrow$  4d transition intensity (eq 3), where  $(1 - \alpha'^2)$  represents the metal 4d contribution to the  $\Psi^*$  orbital.<sup>44</sup>

$$I(\text{metal } 2p \rightarrow \Psi^*) = (1 - \alpha'^2) I(\text{metal } 2p \rightarrow 4d) \quad (3)$$

The pre-edge intensity of the metal L-edge complements the ligand K-edge data and provides a direct probe of the metal contribution  $(1 - \alpha'^2)$  to the unoccupied orbitals in the ligand field manifold. The 2p and 4d spin-orbit and 2p core-hole–4d multiplet interactions may affect the peak intensities of these transitions and must be considered in the analysis of the L<sub>3</sub>- and L<sub>2</sub>-edge spectra.<sup>60</sup>

(60) de Groot, F. M. F.; Hu, Z. W.; Lopez, M. F.; Kaindl, G.; Guillot, F.; Tronc, M. *J. Chem. Phys.* **1994**, *101*, 6570–6576.



Herein, the ligand K- and metal L-edge spectra are reported and analyzed for the diamagnetic Mo(VI) chromophores  $\text{LMo}^{\text{VI}}\text{O}_2\text{X}$  ( $\text{X} = \text{Cl}, \text{SCH}_2\text{Ph}, \text{OPh}$ ). The series includes the benzyl thiolate complex to mimic the Mo–S interaction of cysteine with the Mo center in the sulfite oxidases. The experimental estimates of covalency are compared to density functional calculations for analogues of each complex. These results are used to obtain electronic structure insight into the oxo transfer reactivity for the  $\text{LMo}^{\text{VI}}\text{O}_2\text{X}$  complexes and to evaluate the role of the cysteine S in the function of the active site of the sulfite oxidase family of oxomolybdoenzymes.

## 2. Experimental Section

**2.1. Synthesis.** All reactions were carried out under an argon atmosphere using standard Schlenk line techniques. Tetrahydrofuran (THF) was dried and distilled from sodium and benzophenone. Toluene was dried and distilled from sodium. The compounds  $\text{LMo}^{\text{VI}}\text{O}_2\text{X}$  ( $\text{X} = \text{Cl}, \text{SCH}_2\text{Ph}, \text{OPh}$ ) were prepared according to published methods.<sup>29,30</sup> Sodium benzyl thiolate was prepared as follows. Sodium sand was prepared by rapid stirring of molten sodium (0.250 g, 11 mmol) in toluene (10 mL). After the mixture cooled, the toluene was decanted and the sodium washed with three portions of THF (10 mL). The sodium sand was suspended in THF (20 mL), and benzyl mercaptan (1.76 mL, 15 mmol) was added rapidly. The reaction mixture was stirred for 12 h. The white precipitate was removed by filtration and washed with three portions of THF (25 mL) and then with three portions of diethyl ether (25 mL) and dried under vacuum. Yield was 1.35 g (84%).

**2.2. Sample Preparation.**  $\text{LMoO}_2\text{Cl}$ ,  $\text{LMoO}_2(\text{SCH}_2\text{Ph})$ , and  $\text{LMoO}_2(\text{OPh})$  were ground into a fine powder, which was dispersed as thinly as possible on Mylar tape to minimize the possibility of saturation. The procedure has been verified to minimize saturation effects in the data by systematically testing progressively thinner samples until the observed intensity no longer varies with the thickness of the sample. The Mylar tape contained an acrylic adhesive which was determined to have a level of S, Cl, and Mo contaminants below that which is detectable under the conditions of the XAS measurements. The powder on tape was mounted across the window of an aluminum plate. The samples were prepared in dry, anaerobic atmospheres. A 6.35- $\mu\text{m}$  polypropylene window protected the samples from exposure to air during sample transfer from the glovebox to the experimental He-filled sample chamber.

**2.3. X-ray Absorption Measurements.** XAS data were measured at the Stanford Synchrotron Radiation Laboratory using the 54-pole wiggler beamline 6-2 in a high magnetic field mode of 10 kG with a Ni-coated harmonic rejection mirror and a fully tuned Si(111) double crystal monochromator under ring conditions of 3.0 GeV and 50–100 mA. The entire path of the beam was in a He atmosphere. Details of the optimization of this setup for low-energy studies have been described previously.<sup>50,52</sup>

All XAS measurements were made at room temperature in fluorescence excitation mode.<sup>61,62</sup> For reproducibility, two or three scans were measured for each sample. The maximum of the first pre-edge feature in the S K-edge spectrum of  $\text{Na}_2\text{S}_2\text{O}_3 \cdot 5\text{H}_2\text{O}$  was assigned to 2472.02 eV and was used for energy calibration of the S K- and Mo L-edges. The energy of the Cl K-edge data was calibrated by using the energy of the first edge-region feature of  $\text{Cs}_2\text{CuCl}_4$ . The maximum of this peak was assigned to 2820.20 eV. The scans ranges were 2420–2740 eV for the S K- and Mo  $\text{L}_{3-}$ , 2560–2880 eV for the  $\text{L}_{2-}$ , and 2810–2850 eV for Cl K-edges, with a step size of 0.08 eV in the edge region. The spectrometer energy resolution was  $\sim 0.5$  eV.<sup>48,50</sup> Comparison of the first and second derivatives of the spectra of model compounds measured repeatedly during different experimental sessions indicates a reproducibility in edge position of  $\sim 0.1$  eV.

**2.4. Data Analysis.** A smooth background was removed from all spectra by fitting a polynomial to the pre-edge regions and subtracting

this polynomial from the entire spectrum. Normalizations of the S K-, Cl K-, Mo  $\text{L}_{3-}$ , and Mo  $\text{L}_{2-}$  edge data were accomplished by fitting a flat polynomial or straight line to the post-edge region and normalizing the edge jump to 1.0 at 2490, 2840, 2545, and 2655 eV, respectively.

The splining and normalization procedure for the Cl K-edge spectrum of  $\text{LMoO}_2\text{Cl}$  is complicated by the presence of the Mo  $\text{L}_{1-}$  edge at  $\sim 2866$  eV. Utilizing the whole energy range to 3150 eV, i.e., ignoring the intensity of the Mo  $\text{L}_{1-}$  edge, yielded a normalization, which gave the absolutely lowest limit for the pre-edge intensity, which was lower than the true value by the total edge jump contribution of the Mo  $\text{L}_{1-}$  edge. A maximum pre-edge intensity was obtained by manually rescaling an estimated Cl K-edge-only edge jump from the spectrum, as the narrow Cl K-edge-only data range was too short to enable an accurate spline fit.

Peak fittings of S or Cl K-edge spectra were performed on the normalized data of  $\text{LMoO}_2(\text{SCH}_2\text{Ph})$  with  $\text{Na}(\text{SCH}_2\text{Ph})$  as reference and  $\text{LMoO}_2\text{Cl}$ . The fitting program EDG\_FIT,<sup>63</sup> which utilizes the public domain MINPAK fitting library,<sup>64</sup> was used. Pre-edge features were modeled by pseudo-Voigt line shapes (simple sums of Lorentzian and Gaussian functions). This line shape is appropriate, as the experimental features are expected to be a convolution of the Lorentzian transition envelope<sup>48</sup> and the Gaussian line shape imposed by the spectrometer optics.<sup>50,61</sup> A fixed 1:1 ratio of Lorentzian to Gaussian contributions for the pre-edge feature successfully reproduced the S and Cl K-edge spectral features. For the peak fitting of Mo  $\text{L}_{3-}$  and  $\text{L}_{2-}$  edge spectra, the Lorentzian-to-Gaussian ratio was varied. Best fits were obtained when the Lorentzian component was more than 70%. The rising edge is an arctangent function obtained from fits to the Mo  $\text{L}_{3-}$  and  $\text{L}_{2-}$  edge spectra of Mo foil ( $\text{L}_3 = 2521.01$  and  $\text{L}_2 = 2626.20$  eV).

Fits used in the calculation of pre-edge peak intensity were optimized to reproduce both the data and their second derivatives. The peak intensity was approximated by peak area, calculated as the height  $\times$  full width at half-maximum (fwhm). The standard deviation of the average of the areas was calculated to quantitate the uncertainty of the fit for each sample. Our fit criterion is that  $R_f = \sum[y(\text{data}) - y(\text{fit})]^2 / \sum[y(\text{data})]^2$  should be less than 5%.

There are several possible sources of systematic error in the analysis of these spectra. Normalization procedures can introduce a 1–3% difference in pre-edge peak intensity. This maximum of  $\sim 3\%$  error and the error resulting from the fit procedure discussed above were taken into account in the calculation of pre-edge intensities.

**2.5. DFT Calculations.** Spin-restricted calculations were performed using ADF version 2.0.1 employing the local density approximation formulated by Vosko, Wilk, and Nusair.<sup>65</sup> Nonlocal gradient corrections were included for exchange (Becke<sup>66</sup>) and for correlation (Perdew<sup>67</sup>) effects. Basis functions, core expansion functions, core coefficients, and fit functions for Mo, P, S, Cl, C, N, and O were used as provided from database IV of the ADF suite. This includes Slater type orbital (STO) triple- $\zeta$  basis sets for Mo, P, S, Cl, C, N, and O and a single- $\zeta$  polarization function for P, S, Cl, C, N, and O. The functions used for H were from database I, which includes a single- $\zeta$  STO basis without polarization functions. All core levels (up to 4p for Mo, up to 2p for P, S, Cl, and the 1s for C, N, O) were treated as frozen orbitals and orthogonalized to the valence orbitals with core expansion functions.

The DFT calculations were performed on models in which the nitrogen atoms of the ligand L were replaced by three ammonia molecules and the thiolate and alkoxide ligands were represented by  $\text{SCH}_3$  and  $\text{OCH}_3$ , respectively (Chart 1). The geometry of the  $[(\text{NH}_3)_3\text{MoO}_2(\text{SCH}_3)]^+$  model was based on the crystal structure of  $\text{LMoO}_2(\text{SPh})$ <sup>29</sup> and was idealized to  $C_s$  symmetry. The structure of  $\text{LMoO}_2\text{Cl}$  was assumed to be that of  $\text{LMoO}_2(\text{SCH}_3)$  with substitution of chloride for thiolate. The Mo–Cl distance was obtained by geometry optimiza-

(63) Written by G. N. George at Stanford Synchrotron Radiation Laboratory.

(64) Garbow, B. S.; Hillstom, K. E.; More, J. J. *MINPAK*; Argonne National Laboratory: Argonne, IL, 1980.

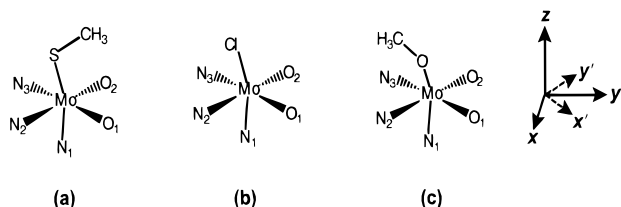
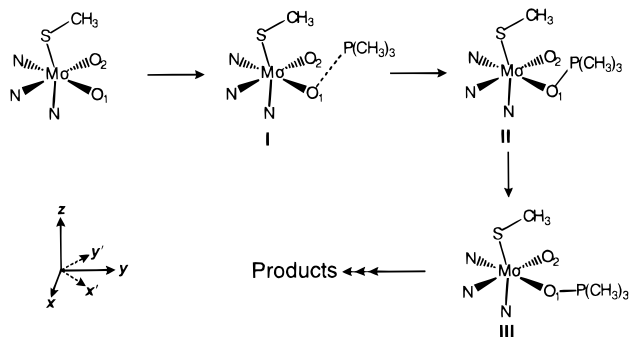
(65) Vosko, S. H.; Wilk, L.; Nusair, M. *Can. J. Phys.* **1980**, *58*, 1200–1211.

(66) Becke, A. D. *Phys. Rev. A* **1988**, *38*, 3098–3100.

(67) Perdew, J. P. *Phys. Rev. B* **1986**, *33*, 8822–8824.

(61) Lytle, F. W.; Greegor, R. B.; Sandstrom, D. R.; Marques, E. C.; Wong, J.; Spiro, C. L.; Huffman, G. P.; Huggins, F. E. *Nucl. Instrum. Methods* **1984**, *226*, 542–548.

(62) Stern, E. A.; Heald, S. M. *Rev. Sci. Instrum.* **1979**, *50*, 1579–1582.

**Chart 1.** Coordinate Systems of  $[(\text{NH}_3)_3\text{MoO}_2(\text{SCH}_3)]^+$  (a),  $[(\text{NH}_3)_3\text{MoO}_2\text{Cl}]^+$  (b), and  $[(\text{NH}_3)_3\text{MoO}_2(\text{OCH}_3)]^+$  (c) for DFT Calculations<sup>a</sup><sup>a</sup> Molecular parameters appear in Table S1 (Supporting Information).**Scheme 2.** Molecular Structures **I**, **II**, and **III** along the Reaction Coordinate for Oxygen Atom Transfer (OAT) from  $[(\text{NH}_3)_3\text{MoO}_2(\text{SCH}_3)]^+$  to  $\text{P}(\text{CH}_3)_3$ <sup>33 a</sup><sup>a</sup> Bond distances and angles for each structure are given in Table S1 (Supporting Information).

tion using a quasi Newton approach.<sup>68</sup> The resultant distance of 2.358 Å is in the range of Mo–Cl distances of 2.35–2.40 Å obtained from a search in the Cambridge Structural Database (CSD)<sup>69</sup> for the *cis*- $\text{Mo}^{\text{VI}}\text{O}_2\text{Cl}$  fragment. The Cl–Mo=O angles are in the range from 95° to 97°. The calculations for  $[(\text{NH}_3)_3\text{MoO}_2(\text{OCH}_3)]^+$  were based on the crystal structure of  $\text{L}'\text{MoO}_2(\text{OCH}_3)$  ( $\text{L}' = \text{hydrotris(3-isopropylpyrazol-1-yl)borate}$ )<sup>29</sup> and employed N–H and C–H distances and H–N–H and H–C–H angles identical to those of  $[(\text{NH}_3)_3\text{MoO}_2(\text{SCH}_3)]^+$ . The coordinate system is rotated by 45° around the *z*-axis from the usual coordinate system for  $\text{O}_h$  complexes. The *yz*-plane is the mirror plane and contains the S–C, Cl,  $\text{O}_{\text{al}}\text{--C}$  ( $\text{O}_{\text{al}}$  = oxygen atom of alkoxide), and  $\text{N}_1$  (axial) atoms. The  $\text{O}_1$  and  $\text{O}_2$  atoms lie in the *xy*-plane, and the *y*-axis bisects the  $\text{O}_1\text{=Mo=O}_2$  angle (Chart 1).

The reactivity of  $\text{LMoO}_2\text{X}$  complexes with phosphines was investigated by DFT calculations of the interactions of the  $[(\text{NH}_3)_3\text{MoO}_2\text{X}]^+$  ( $\text{X} = \text{SCH}_3, \text{Cl}, \text{OCH}_3$ ) models with  $\text{P}(\text{CH}_3)_3$ <sup>70</sup> under three sets of conditions: structure **I**, in which the geometry of the Mo complex was not perturbed, and intermediate structures **II** and **III**, which involved perturbation of the metal center upon interaction of one oxo group with the phosphine (Scheme 2). The parameters for structures **I**, **II**, and **III** were based on the calculations of Pietsch and Hall.<sup>33</sup> The Mo–N distances trans to  $\text{O}_1$  and  $\text{O}_2$  in structures **I**, **II**, and **III** were estimated from the crystal structures of  $\text{L}'\text{MoO}_2(\text{OCH}_3)$ <sup>29</sup> and  $\text{LMoO}(\text{SPh})$  (pyridine).<sup>32</sup> Detailed geometric parameters for the MO calculations are given in Table S1 (Supporting Information).

### 3. Results

#### 3.1. X-ray Absorption Spectroscopy. A. S K-Edge Data.

The normalized S K-edge spectra of  $\text{LMoO}_2(\text{SCH}_2\text{Ph})$  and  $\text{Na}(\text{SCH}_2\text{Ph})$  are shown in Figure 2a. A strong pre-edge feature appears at 2470.5 eV in the spectrum of  $\text{LMoO}_2(\text{SCH}_2\text{Ph})$  which is not present in the spectrum of the  $\text{Na}(\text{SCH}_2\text{Ph})$ . Further, the

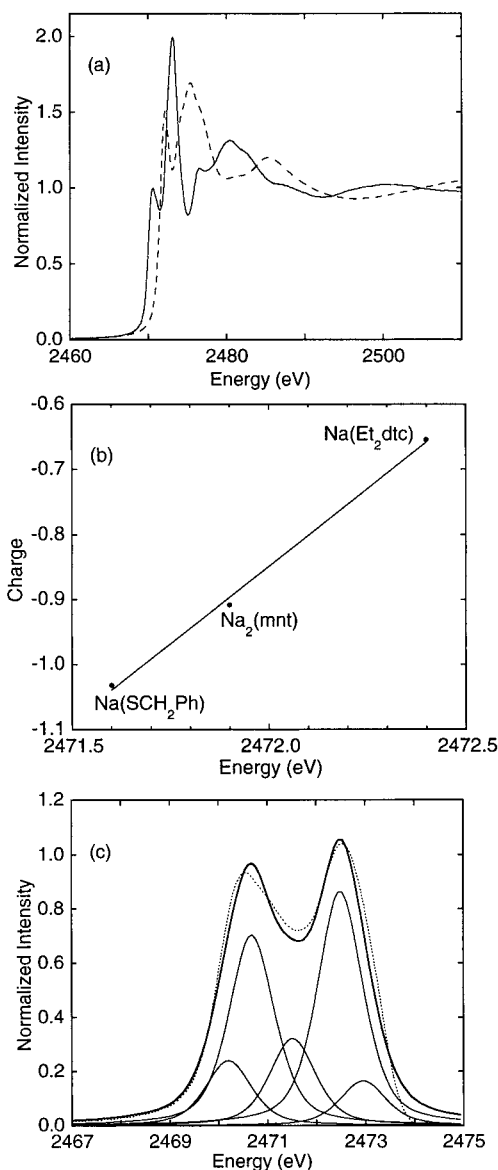


**Figure 2.** (a) Normalized S K-edge spectra of  $\text{LMoO}_2(\text{SCH}_2\text{Ph})$  (solid line) and  $\text{Na}(\text{SCH}_2\text{Ph})$  (dashed line). (b) Relationship between rising edge inflection point of the S K-edge data and the charge (*q*) on the S atom determined by Mulliken population analysis of the DFT calculations for  $\text{Na}(\text{SCH}_2\text{Ph})$ ,  $\text{Na}_2(\text{mnt})$ , and  $\text{Na}(\text{Et}_2\text{dtc})$  ( $q = -1176.3 + 0.47551x$ ,  $R = 0.99864$ ). (c) Difference spectrum (bold solid line) of normalized data for  $\text{LMoO}_2(\text{SCH}_2\text{Ph})$  with an energy shift of +1.3 eV from the  $\text{Na}(\text{SCH}_2\text{Ph})$  data. Representative peak fit (solid lines) and their sum (dotted line).

S K-edge peak at 2473.1 eV of  $\text{LMoO}_2(\text{SCH}_2\text{Ph})$  is more intense than the corresponding feature of  $\text{Na}(\text{SCH}_2\text{Ph})$ , suggesting that some of the intensity in this region of the spectrum results from the overlap of an additional pre-edge feature. The S K-edge spectrum of  $\text{LMoO}_2(\text{SCH}_2\text{Ph})$  contrasts with that of the  $\text{Cu}(\text{II})(\text{d}^9)$ -containing plastocyanin,<sup>50,71,72</sup> which exhibits only one peak at 2469.0 eV. This is consistent with transitions to more than one unoccupied d orbital in the  $\text{Mo}(\text{VI})$  complexes.

The S K-edge of  $\text{Na}(\text{SCH}_2\text{Ph})$  (2471.6 eV) is shifted to lower energy relative to that of  $\text{LMoO}_2(\text{SCH}_2\text{Ph})$ , which is indicative of a greater effective nuclear charge on the S atom in

(68) Fan, L.; Ziegler, T. J. *Chem. Phys.* **1991**, 95, 7401–7408.(69) Allen, F. H.; Kennard, O. 3D Search and reference using the Cambridge Structural Database. *Chem. Des. Autom. News* **1993**, 8, 31.(70) McKean, D. C.; McQuillan, G. P.; Murphy, W. F.; Zerbetto, F. J. *Phys. Chem.* **1990**, 94, 4820–4831.(71) Penfield, K. W.; Gewirth, A. A.; Solomon, E. I. *J. Am. Chem. Soc.* **1985**, 107, 4519–4529.(72) Gewirth, A. A.; Solomon, E. I. *J. Am. Chem. Soc.* **1988**, 110, 3811–3819.

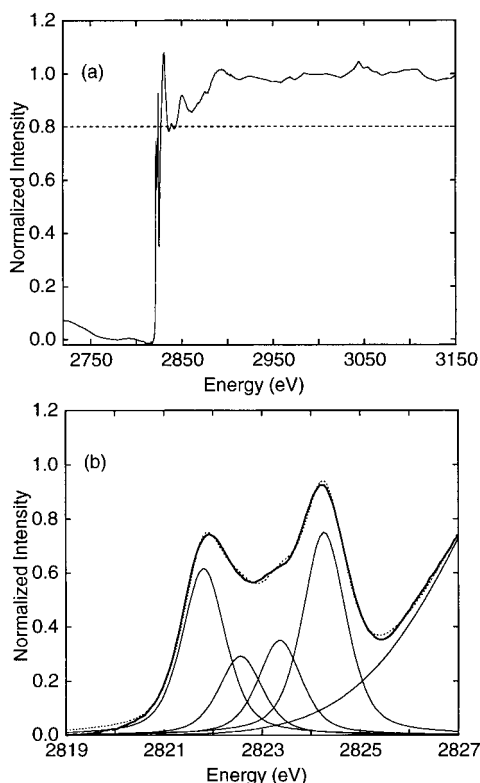


**Figure 3.** (a) Normalized Cl K-edge spectra of LMoO<sub>2</sub>Cl. The spectrum was normalized utilizing the whole energy range to 3150 eV, ignoring the intensity of the Mo L<sub>1</sub> edge at ~2866 eV. The dashed line is a graphical representation of the manual rescaling of an estimated Cl K-edge jump for a maximal pre-edge intensity (see Data Analysis). (b) Representative peak fit (solid lines) and their sum (dotted line).

LMoO<sub>2</sub>(SCH<sub>2</sub>Ph). Prior to background subtraction, the absorption edge of Na(SCH<sub>2</sub>Ph) must be shifted to the absorption edge of LMoO<sub>2</sub>(SCH<sub>2</sub>Ph). An estimate of edge energy can be made through a correlation between the charge on the S atom and the edge position of essentially ionic thiolate salts: Na(SCH<sub>2</sub>Ph), Na<sub>2</sub>(mnt) and Na(Et<sub>2</sub>dtc). A plot of edge energies against the charge on the S atom, estimated from a Mulliken population analysis obtained from DFT calculations, is shown in Figure 2b. DFT calculations on [(NH<sub>3</sub>)<sub>3</sub>MoO<sub>2</sub>(SCH<sub>3</sub>)]<sup>+</sup> give a charge of -0.388 for the S atom. Thus, the absorption edge position for LMoO<sub>2</sub>(SCH<sub>2</sub>Ph) is estimated to be 2472.9 eV, +1.3 eV to higher energy than that for Na(SCH<sub>2</sub>Ph). The difference spectrum of the +1.3 eV-shifted Na(SCH<sub>2</sub>Ph) and LMoO<sub>2</sub>(SCH<sub>2</sub>Ph) spectra is given in Figure 2c and has two major features at 2470.5 and 2472.5 eV, which are assigned as Mo-S pre-edge features. The low-energy feature is substantially broader than the S pre-edge peak of plastocyanin (fwhm ~ 1.7 vs 0.9 eV), indicating that more than one transition contributes to this peak. The total integrated intensity of the pre-edge feature is 2.28.

**B. Cl K-Edge Data.** The Cl K-edge spectrum of LMoO<sub>2</sub>Cl (normalized for the lowest limit of the pre-edge intensity) is shown in Figure 3a. The dashed line gives the estimate for the normalization which yields the highest limit of the pre-edge intensity (see Data Analysis). In contrast to the corresponding S K-edge of LMoO<sub>2</sub>(SCH<sub>2</sub>Ph), the two main pre-edge features at 2821.9 and 2824.2 eV are well separated from the rising edge region. Thus, a background subtraction procedure, as described above, is not necessary. The lower peak is broader than that for [CuCl<sub>4</sub>]<sup>2-</sup> (fwhm ~ 1.6 vs 1.1 eV),<sup>50</sup> indicating that more than one transition contributes to this feature in LMoO<sub>2</sub>Cl. The integrated intensity of the pre-edge features lies between 2.10 and 2.63.

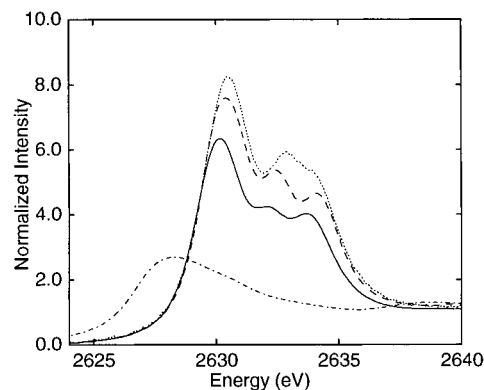


**Figure 4.** Normalized Mo L<sub>2</sub>-edge spectra of LMoO<sub>2</sub>(SCH<sub>2</sub>Ph) (solid line), LMoO<sub>2</sub>Cl (dashed line), LMoO<sub>2</sub>(OPh) (dotted line), and Mo foil (dash-dotted line).

**C. Mo L-Edge Data.** The Mo L<sub>2</sub>-edge spectra of LMoO<sub>2</sub>(SCH<sub>2</sub>Ph), LMoO<sub>2</sub>Cl, LMoO<sub>2</sub>(OPh), and Mo foil are shown in Figure 4. Compared to the featureless spectrum of the Mo foil, the L<sub>2</sub>-edge spectrum of LMoO<sub>2</sub>(SCH<sub>2</sub>Ph) is shifted toward higher energy and exhibits three peaks at 2630.1, 2632.2, and 2633.9 eV. The relatively flat spectrum of the Mo foil may be due to saturation effects associated with the fluorescence detection. The L<sub>2</sub>-edge features of LMoO<sub>2</sub>Cl are at 2630.4, 2632.4, and 2634.1 eV, while those for LMoO<sub>2</sub>(OPh) are at 2630.4, 2632.9, and 2633.9 eV. The splitting between the two higher energy peaks is smaller for LMoO<sub>2</sub>(OPh) than for the other two complexes. The energy splittings within the L<sub>3</sub>-edge spectra of LMoO<sub>2</sub>(SCH<sub>2</sub>Ph), LMoO<sub>2</sub>Cl, and LMoO<sub>2</sub>(OPh) (Supporting Information) are almost identical with those of their respective L<sub>2</sub>-edge spectra. However, the intensities of the lower energy peaks in the L<sub>2</sub>-edge spectra are greater and those of the middle and higher energy peaks are lower compared to the corresponding features in the L<sub>3</sub>-edge spectra. Similar differences in intensity between Mo L<sub>2</sub>/L<sub>3</sub>-edge spectra have also been observed for a variety of inorganic Mo complexes<sup>49,73</sup> and have been associated with the effects of multiplet splitting.<sup>60</sup> Therefore, our analysis focuses on the L<sub>2</sub>-edge features, where these effects are estimated to be small. The total peak intensities of L<sub>2</sub>-edge spectra are in the order LMoO<sub>2</sub>(OPh) > LMoO<sub>2</sub>Cl > LMoO<sub>2</sub>(SCH<sub>2</sub>Ph) (Figure 4).

**3.2. DFT Calculations.** The calculated ligand field splittings for [(NH<sub>3</sub>)<sub>3</sub>MoO<sub>2</sub>X]<sup>+</sup> (X = SCH<sub>3</sub>, Cl, OCH<sub>3</sub>) are shown in Figure 5, and the S 3p, Cl 3p, O<sub>1s</sub> 2p, and Mo 4d characters of the valence orbitals are listed in Table 2. The valence orbitals of the two oxo groups are classified as σ<sub>+</sub>, σ<sub>-</sub>, π<sub>IP</sub>, π<sub>IP</sub>, π<sub>OP</sub>, π<sub>OP</sub>, and π<sub>OP</sub>. The subscripts IP/OP designate in/out of the xy-plane, and the subscripts +/- designate the in-phase and out-of-phase combinations of the 2p orbitals on each oxo group. The σ<sub>+</sub>, σ<sub>-</sub>, π<sub>IP</sub>, π<sub>IP</sub>, π<sub>OP</sub>, π<sub>OP</sub>, and π<sub>OP</sub> orbitals interact with the Mo d<sub>xy</sub>, d<sub>x<sup>2</sup>-y<sup>2</sup></sub>, d<sub>yz</sub>, and d<sub>xz</sub> orbitals, respectively. The π<sub>IP</sub> orbital does not interact with the Mo d orbitals. The bonding is dominated by the interactions of the [MoO<sub>2</sub>]<sup>2+</sup> core, and all three complexes show the same ordering of the Mo 4d orbitals. The d<sub>xy</sub> and d<sub>x<sup>2</sup>-y<sup>2</sup></sub> orbitals, derived from the e<sub>g</sub> set in O<sub>h</sub> symmetry, are most destabilized, with the energy of d<sub>xy</sub> > d<sub>x<sup>2</sup>-y<sup>2</sup></sub>. The d<sub>yz</sub> orbital has a strong antibonding interaction with the oxo σ<sub>-</sub>\* orbital, and the d<sub>xz</sub> orbital has a small contribution from oxo σ<sub>+</sub>\*. The orbitals derived from the t<sub>2g</sub> set in O<sub>h</sub> symmetry have the energy order d<sub>x<sup>2</sup>-y<sup>2</sup></sub> > d<sub>xz</sub> > d<sub>yz</sub>. This order results from a strong

(73) Hedman, B.; Penner-Hahn, J. E.; Hodgson, R. O. In *EXAFS and Near Edge Structure III*, Proceedings of an International Conference, Stanford, CA, July 16–20, 1984; Hedman, B., Penner-Hahn, J. E., Hodgson, K. O., Eds.; Springer-Verlag: Berlin, 1984; pp 64–66.



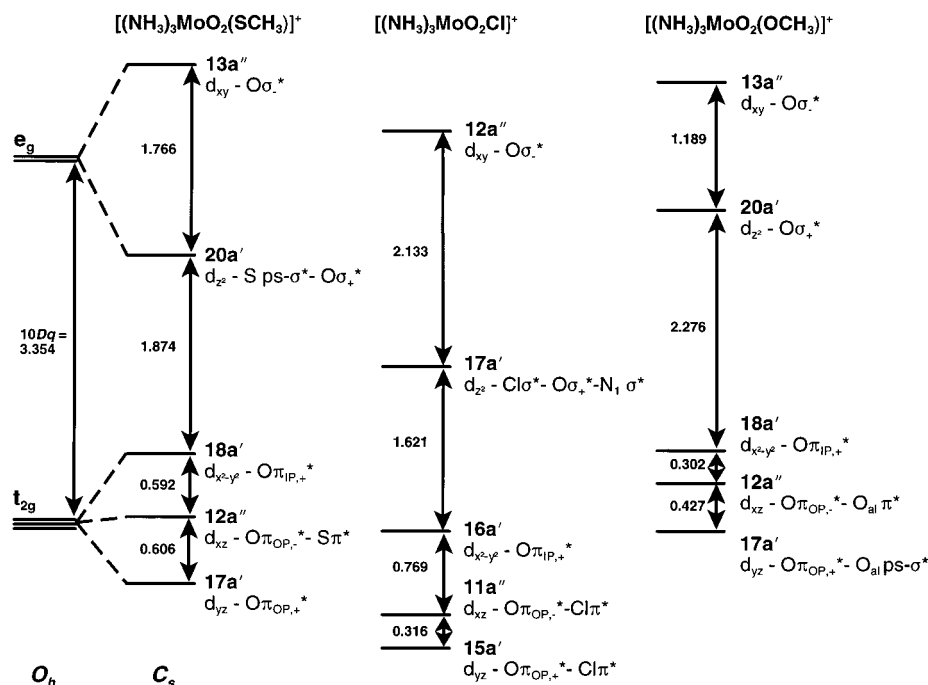


**Figure 5.** Energy diagram of the Mo 4d orbitals and the character for the ground state of  $[(\text{NH}_3)_3\text{MoO}_2(\text{SCH}_3)]^+$ ,  $[(\text{NH}_3)_3\text{MoO}_2\text{Cl}]^+$ , and  $[(\text{NH}_3)_3\text{MoO}_2(\text{OCH}_3)]^+$  obtained by DFT calculations using the geometries of Chart 1. The energy separations between the orbitals are given in electronvolts.

**Table 2.** Comparison of the Mo 4d Orbital Character and Relative Energies for  $[(\text{NH}_3)_3\text{MoO}_2(\text{SCH}_3)]^+$  (A),  $[(\text{NH}_3)_3\text{MoO}_2\text{Cl}]^+$  (B), and  $[(\text{NH}_3)_3\text{MoO}_2(\text{OCH}_3)]^+$  (C) by DFT Calculations

| (A) $[(\text{NH}_3)_3\text{MoO}_2(\text{SCH}_3)]^+{}^a$ |  |   |  |   |   |
|---|--|---|--|---|---|
| orbital character                                       | 17a'<br>$\text{d}_{yz}-\text{O } \pi^*$  | 12a''<br>$\text{d}_{xz}-\text{O } \pi^*-\text{S } \pi^*$            | 18a'<br>$\text{d}_{x^2-y^2}-\text{O } \pi^*$ | 20a'<br>$\text{d}_{z^2}-\text{S pseudo-}\sigma^*-\text{O } \sigma^*$                | 13a''<br>$\text{d}_{xy}-\text{O } \sigma^*$ |
| S 3p character (%)                                      | 2.90   | 11.69   | 3.44   | 17.50   | 0.74  |
| Mo 4d character (%)                                     | 58.74  | 54.89   | 54.83  | 31.99   | 50.15                                       |
| relative energy (eV)                                    | 0  | 0.606   | 1.198  | 3.072   | 4.838                                       |
| (B) $[(\text{NH}_3)_3\text{MoO}_2\text{Cl}]^+{}^b$      |  |   |  |   |   |
| orbital character                                       | 15a'<br>$\text{d}_{yz}-\text{O } \pi^*-\text{Cl } \pi^*$                             | 11a''<br>$\text{d}_{xz}-\text{O } \pi^*$                            | 16a'<br>$\text{d}_{x^2-y^2}-\text{O } \pi^*$ | 17a'<br>$\text{d}_{z^2}-\text{O } \sigma^*-\text{Cl } \sigma^*-\text{N}_1 \sigma^*$ | 12a''<br>$\text{d}_{xy}-\text{O } \sigma^*$ |
| Cl 3p character (%)                                     | 10.03  | 4.89  | 2.26   | 12.05   | 0.20  |
| Mo 4d character (%)                                     | 58.76  | 57.65   | 56.24  | 48.94   | 51.48                                       |
| relative energy (eV)                                    | 0  | 0.316   | 1.085  | 2.706   | 4.839                                       |
| (C) $[(\text{NH}_3)_3\text{MoO}_2(\text{OCH}_3)]^+{}^c$ |  |   |  |   |   |
| orbital character                                       | 17a'<br>$\text{d}_{yz}-\text{O } \pi^*-\text{O}_{\text{al}} \text{ pseudo-}\sigma^*$ | 12a''<br>$\text{d}_{xz}-\text{O } \pi^*-\text{O}_{\text{al}} \pi^*$ | 18a'<br>$\text{d}_{x^2-y^2}-\text{O } \pi^*$ | 20a'<br>$\text{d}_{z^2}-\text{O } \sigma^*$   | 13a''<br>$\text{d}_{xy}-\text{O } \sigma^*$ |
| O <sub>al</sub> 2p character (%)                        | 10.68  | 8.21  | 0.20   | 3.35  | 0   |
| Mo 4d character (%)                                     | 58.44  | 57.22   | 55.86  | 50.47   | 48.92                                       |
| relative energy (eV)                                    | 0  | 0.427   | 0.729  | 3.005   | 4.194                                       |

<sup>a</sup> The summation of S 3p character across five orbitals is 36.27% (total S 3p character). <sup>b</sup> The summation of Cl 3p character across five orbitals is 29.43% (total Cl 3p character). <sup>c</sup> The summation of O 2p character across five orbitals is 22.44% (total O<sub>al</sub> 2p character).

interaction between the  $\text{d}_{x^2-y^2}$  and  $\text{oxo } \pi_{\text{IP},+}^*$  orbitals and from a greater overlap of  $\text{d}_{xz}$  with  $\text{oxo } \pi_{\text{OP},-}^*$  compared to  $\text{d}_{yz}$  with  $\pi_{\text{OP},-}^*$ , due to the  $\text{O}=\text{Mo}=\text{O}$  angle ( $\sim 103^\circ$ ).

The splittings of the Mo 4d orbitals are further modulated by anisotropic bonding interactions with the X ligand, as shown in Figure 5 and the representative contour plots of Figure 6. The  $16^\circ$  tilt of the Mo–X bond from the z-axis introduces bonding anisotropy that is common to all X ligands (Figure 7). For X = Cl, the three 3p orbitals of Cl can form one  $\sigma$  and two  $\pi$  bonds to Mo, and the only perturbing factor is the tilt of the Mo–Cl bond. The Cl  $\sigma$  is antibonding to the  $\text{d}_{z^2}$  orbital. The Cl  $\pi^*$  overlap with the  $\text{d}_{yz}$  orbital (Figure 6d, Table 2B) is more than twice the Cl  $\pi^*$  contribution that destabilizes the  $\text{d}_{xz}$  orbital (Figure 6e). For X = SCH<sub>3</sub>, one of the three 3p orbitals of the S atom of the thiolate ligand is used for S–C bonding, and the

remaining two are available for  $\pi$  and pseudo- $\sigma$  bonding to the Mo. The term pseudo- $\sigma$  is associated with the deviation of the C–S–Mo angle ( $105.8^\circ$ ) from  $90^\circ$ .<sup>74</sup> The S pseudo- $\sigma^*$  orbital interacts primarily with the  $\text{d}_{z^2}$  orbital (Figure 6c), but there are also small contributions of the S pseudo- $\sigma^*$  to the  $\text{d}_{yz}$  (Figure 6a) and the  $\text{d}_{x^2-y^2}$  orbitals. The thiolate  $\pi^*$  orbital overlaps principally with  $\text{d}_{xz}$  (Figure 6b), in contrast to X = Cl, and thereby increases the splitting between the  $\text{d}_{yz}$  and  $\text{d}_{xz}$  orbitals already induced by the overlap difference with  $\pi_{\text{OP},+}^*$  and  $\pi_{\text{OP},-}^*$ , respectively. The anisotropy of the thiolate  $\pi^*$  interaction with  $\text{d}_{xz}$  and  $\text{d}_{yz}$  also varies with the Mo–S–CH<sub>3</sub> torsional angle (Figure 8). For X = OCH<sub>3</sub>, the bonding is similar to that for SCH<sub>3</sub>; the three 2p orbitals of the O<sub>al</sub> are used in O<sub>al</sub>–C bonding

(74) Gebhard, M. S.; Deaton, J. C.; Koch, S. A.; Millar, M.; Solomon, E. I. *J. Am. Chem. Soc.* **1990**, *112*, 2217–2231.



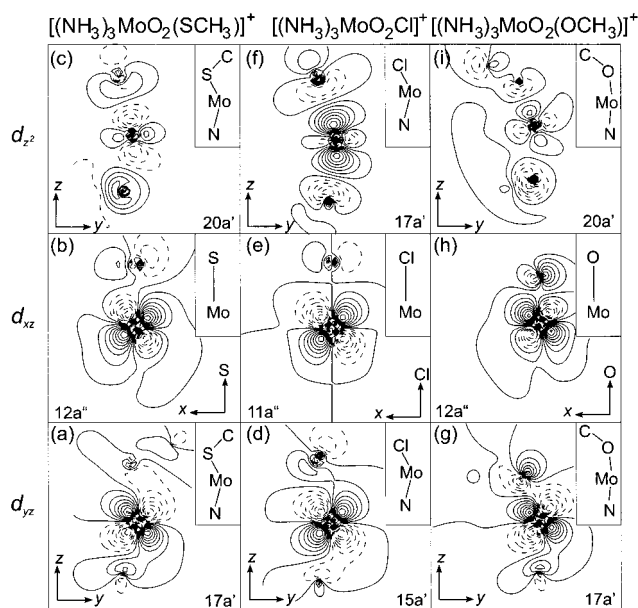


**Figure 6.** ADF contour plots of 17a' ( $d_{yz}$ ) (a), 12a'' ( $d_{xz}$ ) (b), 20a' ( $d_{z^2}$ ) (c) for  $[(\text{NH}_3)_3\text{MoO}_2(\text{SCH}_3)]^+$ ; 15a' ( $d_{yz}$ ) (d), 11a'' ( $d_{xz}$ ) (e), 17a' ( $d_{z^2}$ ) (f) for  $[(\text{NH}_3)_3\text{MoO}_2\text{Cl}]^+$ ; 17a' ( $d_{yz}$ ) (g), 12a'' ( $d_{xz}$ ) (h), 20a' ( $d_{z^2}$ ) (i) for  $[(\text{NH}_3)_3\text{MoO}_2(\text{OCH}_3)]^+$ .

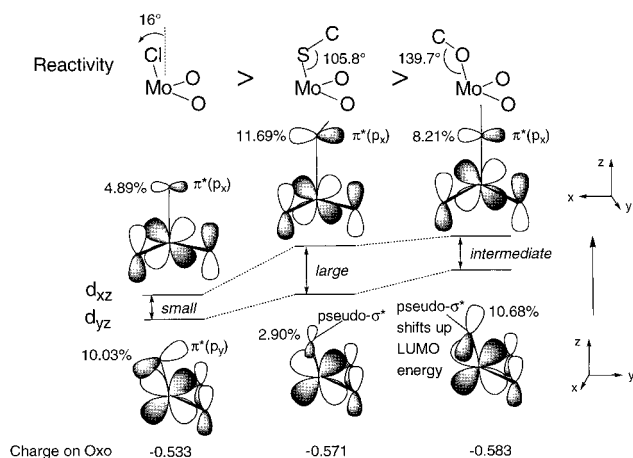


**Figure 7.** Energies and pictorial representations of the principal interactions of the  $d_{yz}$  and  $d_{xz}$  orbitals with the oxo  $\pi_{\text{OP},-}$  and  $\pi_{\text{OP},+}$  sets and the Cl, S,  $\text{O}_{\text{al}}$  ligands.

and in  $\sigma$  and  $\pi$  bonding to Mo. The alkoxide  $\pi^*$  interacts with the  $d_{xz}$  orbital (Figure 6h). The  $\text{C}-\text{O}_{\text{al}}-\text{Mo}$  angle of  $139.7^\circ$  leads to overlap of the  $\text{O}_{\text{al}}$  pseudo- $\sigma^*$  orbital with the  $d_{yz}$  orbital (Figure 6g, Table 2C) that is more than 3 times larger than the overlap with the  $d_{z^2}$  orbital (Figure 6i). This orbital composition contrasts with that for  $\text{X} = \text{SCH}_3$ , where the dominant S pseudo- $\sigma^*$  overlap is with the  $d_{z^2}$  orbital (Figure 6c).

The calculated total covalency of the  $\text{Mo}-\text{X}$  bond for the three  $[(\text{NH}_3)_3\text{MoO}_2\text{X}]^+$  complexes increases in the order  $\text{Mo}-\text{OCH}_3 < \text{Mo}-\text{Cl} < \text{Mo}-\text{SCH}_3$  (Table 2). The energy of the redox-active orbital depends on  $\text{X}$  [ $\text{Cl}$  ( $-8.326$ )  $<$   $\text{SCH}_3$  ( $-7.724$ )  $<$   $\text{OCH}_3$  ( $-7.229$  eV)], but the Mo  $4d_{yz}$  character of the orbital is similar for all three complexes. The estimated charge on the Mo ion from a Mulliken population analysis for  $\text{X} = \text{Cl}$  ( $+2.242$ ) and  $\text{X} = \text{SCH}_3$  ( $+2.207$ ) is consistent with the energy order.<sup>75</sup> However, the estimated higher charge on Mo for  $\text{X} = \text{OCH}_3$  ( $+2.432$ ) does not lower the energy of the redox-active orbital. Rather, it is the significant overlap of the

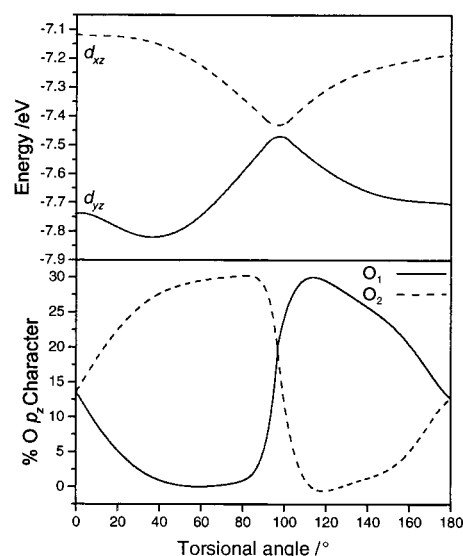


**Figure 8.** (a) Calculated Mo  $d_{yz}$  and  $d_{xz}$  orbital energy changes and (b) calculated  $\text{O}_1$  and  $\text{O}_2$   $p_z$  character when the methyl group of the thiolate is rotated around the  $\text{Mo}-\text{S}$  bond for  $[(\text{NH}_3)_3\text{MoO}_2(\text{SCH}_3)]^+$ . This torsional angle is measured relative to the  $yz$  plane and is in an anticlockwise sense.

$\text{O}_{\text{al}}$  pseudo- $\sigma^*$  orbital with the  $d_{yz}$  orbital that shifts it to highest energy. The energy splitting of the  $d_{yz}$  and  $d_{xz}$  orbitals is determined by anisotropic contributions from S, Cl, or  $\text{O}_{\text{al}}$  in addition to the strong  $\pi_{\text{IP/OP}}$  bonds from the two oxo groups. The splitting is largest (0.606 eV) for  $\text{X} = \text{SCH}_3$ , where the  $d_{xz}$  orbital is further destabilized by a S  $\pi^*$  interaction; intermediate (0.427 eV) for  $\text{X} = \text{OCH}_3$ , where both the  $d_{xz}$  and  $d_{yz}$  orbitals are destabilized by  $\text{O}_{\text{al}}$  pseudo- $\sigma^*$  and  $\pi^*$  contributions; and smallest (0.316 eV) for  $\text{X} = \text{Cl}$ , where the  $d_{yz}$  orbital is destabilized by a Cl  $\pi^*$  interaction (Figure 7).

#### 4. Analysis: Peak Fit and Spectral Assignments

**A. S K-Edge.** The two strong peaks in the difference spectrum of  $\text{LMoO}_2(\text{SCH}_2\text{Ph})$  (Figure 2c) were first modeled with only two peaks. The fwhm were fixed in the range of 0.9–1.1 eV, values that have been observed for the pre-edge of plastocyanin.<sup>50,53</sup> The difference of the spectrum and this two-peak model gives rise to three additional features, a stronger one in the center and two weaker ones at the sides. A reasonable simulation with this five-peak model is shown in Figure 2c, and the peak areas and energies are listed in Table 3A. Due to the subtraction procedure described in the Results section, the energies and intensities can only be analyzed in a qualitative manner, but the total intensity is reasonable.

Using the DFT calculations as a guide, the two strong peaks at 2470.7 and 2472.5 eV can be assigned as transitions to the  $d_{xz}-\text{S } \pi^*$  (12a'') and  $d_{z^2}-\text{S pseudo-}\sigma^*$  (20a') orbitals, respectively (Figure 5). The splitting is found to be 1.8 eV, supporting the calculated orbital splitting of  $d_{xz}$  and  $d_{z^2}$  (2.47 eV), assuming a final state reduction of  $\sim 0.7$ . The other three weaker peaks, at 2470.2, 2471.5, and 2472.5 eV, are assigned to S pseudo- $\sigma^*$  contributions to  $d_{yz}$  (17a'),  $d_{x^2-y^2}$  (18a'), and  $d_{xy}$  (13a'') respectively, based on their energies and low peak intensities in comparison to the coefficients in Table 2A. The peak areas and energies (Table 3A) are in qualitative agreement with the S 3p character in the five Mo 4d orbitals obtained from the DFT calculations (Table 2A). The differences are due to final state relaxation effects; e.g., the electron–electron repulsion contribution in the final state relaxation varies for different transitions due to differences in delocalization over the ligands. Addition-

(75) Cimino, A.; de Angelis, B. A. *J. Catal.* **1975**, *36*, 11–22.

**Table 3.** Average Deconvoluted Peak Area and Energy from S K- and Cl K-Edges for Oxomolybdenum Complexes

| edge     | sample   |                    | peak           |                |                |                |                | total |
|----------|--|--------------------|----------------|----------------|----------------|----------------|----------------|-------|
|          |  |                    | 1              | 2              | 3              | 4              | 5              |       |
| (A) S K  | LMoO <sub>2</sub> (SCH <sub>2</sub> Ph) <sup>a</sup> | area               | 0.24 ± 0.01    | 0.70 ± 0.08    | 0.32 ± 0.05    | 0.86 ± 0.04    | 0.16 ± 0.04    | 2.28  |
|          |  | energy (eV)        | 2470.20 ± 0.06 | 2470.68 ± 0.06 | 2471.51 ± 0.04 | 2472.49 ± 0.02 | 2472.95 ± 0.02 |       |
|          |  | relative to peak 1 | 0              | 0.48           | 1.31           | 2.29           | 2.75           |       |
|          |  |                    |                |                |                |                |                |       |
| (B) Cl K | LMoO <sub>2</sub> Cl <sup>b</sup>                    | area               | 0.65 ± 0.02    | 0.31 ± 0.07    | 0.34 ± 0.03    | 0.79 ± 0.04    |                | 2.10  |
|          |  | energy (eV)        | 2821.81 ± 0.01 | 2822.56 ± 0.09 | 2823.36 ± 0.15 | 2824.27 ± 0.04 |                |       |
|          |  | relative to peak 1 | 0              | 0.75           | 1.55           | 2.46           |                |       |
|          |  |                    |                |                |                |                |                |       |

<sup>a</sup> The errors given for the S K-edge fitting are for the fitting procedure to the difference spectrum obtained from the correlation described in the Results section. <sup>b</sup> The areas of the Cl pre-edge peaks are given for the lowest intensity limit for pre-edge intensity (see text). The highest intensity limit is obtained by multiplying by 1.25.

ally, the subtraction procedure yields large uncertainties, especially for the higher energy part of the pre-edge.

To quantify the covalency, an equation relating the experimentally observed pre-edge intensity ( $D_0$ ) to ligand covalency for the d<sup>0</sup> system, based on the dipole strength expressions of ref 52, is given in eq 4. This dipole strength expression for the intensity of a ligand K-edge transition for metal ions with only one parent excited state is<sup>52</sup>

$$D_0 = \left( \frac{h_{t_2}}{3} c_{t_2}^2 + \frac{h_e}{3} c_e^2 \right) \langle s|r|p \rangle^2 \quad (4)$$

where  $h_{t_2}$  and  $h_e$  are the number of holes in the  $t_2$  and  $e$  orbitals, respectively,  $c_{t_2}^2$  and  $c_e^2$  are the ligand characters in the  $t_2$  and  $e$  orbitals, respectively, and  $\langle s|r|p \rangle$  is the transition moment integral. The simple form of eq 4 derives from the weak coupling of the ligand 1s core hole with the metal ion final states. For a d<sup>0</sup> system  $h_{t_2} = 6$  and  $h_e = 4$ . Note that while, in ref 52a, only tetrahedral complexes were analyzed, octahedral complexes may also be treated with this methodology. Thus,  $c_{t_{2g}}^2$  and  $c_{e_g}^2$  become the ligand  $\pi$ - and  $\sigma$ -covalencies in the  $t_{2g}$  and  $e_g$  orbitals, respectively.

Application of eq 4 to the total S K pre-edge intensity of LMoO<sub>2</sub>(SCH<sub>2</sub>Ph), using plastocyanin (renormalized intensity 1.02; 38% thiolate covalency)<sup>50,76</sup> as the reference, yields a total covalency, i.e., the total contribution of the thiolate ligand to the five Mo d orbitals, of ~42%. This value is 1.2 times greater than the total covalency obtained from the molecular orbital calculation (36%, Table 2A).

In summary, the two main S K-edge peaks are assigned as S 1s transitions to the  $d_{xz}$ -S  $\pi^*$  and  $d_{yz}$ -S pseudo- $\sigma^*$  molecular orbitals. The additional weak features are assigned to the  $d_{yz}$ ,  $d_{x^2-y^2}$ , and  $d_{xy}$  orbitals, which have some limited overlap with the S pseudo- $\sigma^*$  orbital.

**B. Cl K-Edge.** The spectrum of LMoO<sub>2</sub>Cl (Figure 3) shows at least three features in the pre-edge region, two strong peaks 2821.8 and 2824.3 eV and some intensity in the region between these peaks. Fits with only three pre-edge peaks do not well reproduce the region between the two strong peaks. Four peak models fit the absorption data and their second derivative. The average peak areas and energies are listed in Table 3B, and a representative fit is shown in Figure 3b. These values are more reliable than the corresponding S K-edge values because no subtraction procedure was necessary for the Cl K-edge.

The two distinct peaks at 2821.8 and 2824.3 eV are assigned as Cl 1s transitions to the  $d_{yz}$ -Cl  $\pi^*$  (15a') and  $d_{z^2}$ -Cl  $\sigma^*$  (17a') levels, respectively, using the DFT calculations as a benchmark (Figure 5). The splitting is 2.5 eV, which is consistent with the

orbital splitting of 2.71 eV from the ground-state calculations, assuming a final state relaxation factor of ~0.9. The two weaker peaks at 2822.6 and 2823.4 eV are assigned as transitions to the Cl  $\pi^*$  component of  $d_{xz}$  and the Cl  $\sigma^*$  component of the  $d_{x^2-y^2}$  levels, respectively, on the basis of their energies relative to two main peaks and their reduced peak intensities. The ratios of peak areas (Table 3B) are in reasonable agreement with the relative Cl 3p character in four Mo 4d orbitals from the DFT calculations (Table 2B). The Cl 3p character in the  $d_{xy}$  orbital is negligible, supporting the four-peak fit.

The measured intensity of the pre-edge feature of the Cl K-edge (2.1–2.6) yields [using eq 4 and  $D_{2d}[\text{CuCl}_4]^{2-}$  (normalized intensity 0.526, 30% Cl covalency<sup>48,50</sup>)<sup>76</sup> as the reference for calculation of the transition moment integral] a total covalency over the five d orbitals of 15–19%. The covalency obtained from the DFT calculation is ~29%. Because the structure of [LMoO<sub>2</sub>Cl] is not known, DFT calculations were also performed on structures with varying Mo–Cl distances (up to 2.6 Å) and changes in the tilt angle of the Mo–Cl vector (from 0 to 16°). The calculated covalency varied by only a few percent. DFT calculations using the ADF program suite on mono- and binuclear iron chloride and thiolate complexes also give an overestimation of the covalency for chloride and an underestimation for sulfur ligation relative to experimental values.<sup>77</sup>

**C. Mo L<sub>2</sub>-Edge.** The peak fits and spectral assignments for the Mo L<sub>2</sub>-edge data are given in the Supporting Information.

## 5. Discussion

**5.1. Description of the Bonding in [(NH<sub>3</sub>)<sub>3</sub>MoO<sub>2</sub>X]<sup>+</sup> (X = SCH<sub>3</sub>, Cl, and OCH<sub>3</sub>) and Relation to Spectroscopic Data.** The DFT calculations for the model dioxomolybdenum complexes [(NH<sub>3</sub>)<sub>3</sub>MoO<sub>2</sub>X]<sup>+</sup> (X = SCH<sub>3</sub>, Cl, and OCH<sub>3</sub>) show the same calculated energy order of the five Mo 4d orbitals for all three complexes ( $d_{yz} < d_{xz} < d_{x^2-y^2} < d_{z^2} < d_{xy}$ ), consistent with the two *cis*-oxo groups dominating the ligand field (Figure 5, section 3.2). The energies are further perturbed by additional covalent contributions from the X ligand. The splitting of the  $d_{xz}$  and  $d_{yz}$  orbitals increases in the order Cl < O<sub>al</sub> < S, and the major perturbing factor is the presence of the CH<sub>3</sub> group in the thiolate and alkoxide ligands, which essentially eliminates one of the valence  $\pi$  orbitals from bonding to the Mo d orbitals. The Mo–X–CH<sub>3</sub> torsional angle and the Mo–X–CH<sub>3</sub> bond angles further modulate the overlap of the remaining pseudo- $\sigma$  and  $\pi$  orbitals with the Mo 4d orbitals (Figures 6 and 8). The key orbital interactions with X are the following: Cl  $\pi^*$  to  $d_{yz}$  and Cl  $\sigma^*$  to  $d_{z^2}$  for X = Cl; S  $\pi^*$  to  $d_{xz}$  and S pseudo- $\sigma^*$  to  $d_{z^2}$  for X = SCH<sub>3</sub>; O<sub>al</sub>  $\pi^*$  to  $d_{xz}$  and O<sub>al</sub> pseudo- $\sigma^*$  to  $d_{xz}$  for X = OCH<sub>3</sub>. The Cl and S K-edge spectra provide experimental proof of the two dominant (pseudo- $\sigma^*$  and  $\pi^*$ ) contributions to metal–

(76) Note that the renormalization intensities used for the chloride and thiolate pre-edge involve normalization of the edge jump for each ligand and thus can be compared for the same ligand type but not between different ligand types.

(77) Glaser, T.; Kennepohl, P.; Solomon, E. I. Unpublished results.

ligand covalency in  $\text{LMoO}_2\text{X}$  compounds. The Mo  $L_2$ -edge spectra reflect the trend of total covalency of Cl, S, and O<sub>al</sub> with Mo:  $\text{LMoO}_2(\text{SCH}_2\text{Ph}) \geq \text{LMoO}_2\text{Cl} > \text{LMoO}_2(\text{OPh})$ .

**5.2. Correlation to Reactivity. A. Reduction Potential.** The data in Table 1 show that the nature of X influences the one-electron reduction potential of  $\text{LMoO}_2\text{X}$  complexes ( $\text{Mo}^{\text{VI}} \rightarrow \text{Mo}^{\text{V}}$ ) as well as the rates of the two-electron reduction ( $\text{Mo}^{\text{VI}} \rightarrow \text{Mo}^{\text{IV}}$ ) that occurs during the OAT reaction of these complexes with  $\text{PPh}_3$ . The following sections consider each of these properties in light of the spectroscopic and theoretical investigations of these systems described above.

There are several factors that influence redox potentials in solution. These include the effective nuclear charge on the metal ion, the energy of the redox-active orbital, and electronic relaxation.<sup>78</sup> With increasing charge at the metal center, reduction should be easier; i.e., the reduction potential should increase. The effective nuclear charge on the Mo in the  $[(\text{NH}_3)_3\text{MoO}_2\text{X}]^+$  analogues was estimated from a Mulliken population analysis of the DFT results and the application of Slater's rules (+4.67 for X =  $\text{SCH}_3$ , +4.68 for X = Cl, and +4.75 for X =  $\text{OCH}_3$ ). There is no correlation between these calculated effective nuclear charges and the experimental reduction potentials of Table 1. However, the calculated energies of the redox active orbital ( $d_{yz}$ , Figure 5: -8.326 for X = Cl, -7.724 for X =  $\text{SCH}_3$ , and -7.229 eV for X =  $\text{OCH}_3$ ) correlate well with the experimental reduction potentials. The significant interaction with the O<sub>al</sub> pseudo- $\sigma^*$  destabilizes the  $d_{yz}$  orbital and makes the dominant contribution to the low reduction potential of X =  $\text{OCH}_3$ .

Geometric and electronic structural changes on reduction can also contribute to the reduction potential of a metal complex. For the  $[\text{LMoO}_2(\text{SPh})]^{0/-}$  pair, the reduced  $\text{Mo}^{\text{V}}$  species has longer M=O and Mo-S distances and a larger O=Mo=O angle.<sup>79</sup> DFT calculations on a  $[(\text{NH}_3)_3\text{Mo}^{\text{VO}}_2(\text{SCH}_3)]^0$  model idealized to  $C_s$  symmetry showed that interactions between the oxo groups and the Mo 4d orbitals dominate the ligand field such that the 4d orbital energy order of the  $\text{Mo}^{\text{VI}}$  complex (Figure 5, left-hand side) is conserved in the  $\text{Mo}^{\text{V}}$  complex. The major contributions from S are  $\pi^*$  (6.18%) to the  $d_{xz}$  orbital and pseudo- $\sigma^*$  (17.16%) to the  $d_{z^2}$  orbital. Although the calculated Mo-S covalency for the  $\text{Mo}^{\text{V}}$  complex is less than that for the  $\text{Mo}^{\text{VI}}$  thiolate complex (Table 2A), the general bonding description is the same. Thus, it is reasonable to infer that the experimental order of the reduction potentials ( $\text{Cl} > \text{SCH}_2\text{Ph} > \text{OCH}_3$ ) reflects the differences in the anisotropic covalent bonding interactions of the axial chloride, thiolate, and alkoxide ligands upon the energy of the redox-active orbital.

**B. Oxo Transfer Reactivity.** Oxygen atom transfer (OAT) from the  $\text{cis-}[\text{Mo}^{\text{VI}}\text{O}_2]^{2+}$  fragment to sulfite is proposed for the first step in the catalytic cycle of sulfite oxidase (Scheme 1).<sup>19</sup> Reactions of  $\text{LMo}^{\text{VI}}\text{O}_2\text{X}$  (X = Cl, SPh, OPh,  $\text{OCH}_3$ ) with  $\text{PPh}_3$  mimic this OAT functionality, with the observed rate order being  $\text{Cl} > \text{SPh} > \text{OPh} > \text{OCH}_3$  (Table 1) for the reduction of  $\text{LMo}^{\text{VI}}\text{O}_2\text{X}$  to "LMo<sup>IV</sup>OX" and oxidation of  $\text{PPh}_3$  to  $\text{OPPh}_3$ .

A theoretical model, employing Hartree-Fock and Møller-Plesset perturbation theory, has been used to propose intermediates for both the oxo transfer step and the subsequent displacement of the  $\text{OPPh}_3$  product by water.<sup>33</sup> The energetics of the reaction pathway were probed using  $\text{P}(\text{CH}_3)_3$  and  $\text{cis-}[(\text{NH}_3)_2\text{MoO}_2(\text{SH})_2]^0$  as the model complex and by consideration of

one possible reaction mechanism for oxo transfer.<sup>36,80</sup> The geometries of the intermediates were optimized at the restricted Hartree-Fock level and reveal that  $\text{P}(\text{CH}_3)_3$  approaches one O atom of  $\text{cis-}[(\text{NH}_3)_2\text{MoO}_2(\text{SH})_2]^0$  at a O=Mo=O-P dihedral angle of approximately  $90^\circ$  and at a Mo=O-P angle of  $130.7^\circ$ . A weak P-O interaction develops ( $\text{P}\cdots\text{O} = 2.43 \text{ \AA}$ ) at the top of an activation barrier of  $14 \text{ kcal mol}^{-1}$ . Rotation of the  $\text{P}(\text{CH}_3)_3$  group about the Mo-O bond to a O=Mo=O-P dihedral angle of  $0^\circ$  generates a  $\text{Mo}(\text{IV})$  intermediate that is approximately  $69 \text{ kcal mol}^{-1}$  lower in energy due to the formation of a P=O bond. Displacement of  $\text{OP}(\text{CH}_3)_3$  by water in an associative step completes the OAT process.<sup>33</sup>

The bonding changes that occur in  $\text{LMo}^{\text{VI}}\text{O}_2\text{X}$  (X = Cl,  $\text{SCH}_2\text{Ph}$ , OPh) along a reaction coordinate for OAT to  $\text{PPh}_3$  have been explored by DFT calculations. The geometries of the reaction intermediates are based upon the estimates of Pietsch and Hall,<sup>33</sup> and frontier orbital theory is used to rationalize the relative rates of the OAT reaction of  $\text{LMo}^{\text{VI}}\text{O}_2\text{X}$  with  $\text{PPh}_3$ . Scheme 2 illustrates structures **I**–**III** along a coordinate for the reaction of the  $[(\text{NH}_3)_3\text{MoO}_2(\text{SCH}_3)]^+$  model with  $\text{P}(\text{CH}_3)_3$ . Structure **I** corresponds to the reactants before significant reaction, structure **II** to the transition state, and structure **III** to the  $\text{Mo}^{\text{IV}}\text{O}(\text{OP}(\text{CH}_3)_3)$  intermediate in the scheme of Pietsch and Hall.<sup>33</sup>

The energies of the HOMO (the lone pair of the attacking P atom) and the LUMO ( $\text{Mo } d_{yz} - \sigma_{\text{OP},+}^*$ ) for structures **I** and **II** and the HOMO for structure **III** are illustrated in Figure 9. Before reaction with  $\text{P}(\text{CH}_3)_3$ , the major contribution of X to the  $d_{yz}$  and  $d_{xz}$  orbitals is Cl  $\pi^*$  to  $d_{yz}$  (X = Cl), S  $\pi^*$  to  $d_{xz}$  (X = S), and O<sub>al</sub> pseudo- $\sigma^*$  to  $d_{yz}$  and O<sub>al</sub>  $\pi^*$  to  $d_{xz}$  (X = O) (Figure 7). In the frontier orbital theory model, the energy change ( $\Delta E$ ) when the HOMO of a nucleophile interacts with the LUMO of an electrophile is formulated as follows:

$$\Delta E = -\frac{Q_{\text{nucleophile}}Q_{\text{electrophile}}}{\epsilon R} + \frac{2(c_{\text{nucleophile}}c_{\text{electrophile}}\beta)^2}{E_{\text{HOMO(nucleophile)}} - E_{\text{LUMO(electrophile)}}} \quad (5)$$

where  $Q$  is the charge of reacting atom,  $\epsilon$  is the local dielectric constant,  $R$  is the distance between the two reacting atoms,  $c$  is the coefficient of the atomic orbital of the reacting atom in the molecular orbital, and  $\beta$  is the resonance integral for the two wave functions corresponding to the  $c_{\text{nucleophile}}$  and  $c_{\text{electrophile}}$  coefficients.<sup>81</sup> This perturbation theory approach cannot be used to estimate the activation energy of the first step of the OAT reaction. Nevertheless, it does provide an estimate of the change in energy ( $\Delta E$ ) over the early part of the reaction coordinate.

The first term in eq 5 represents the Coulombic attraction between the two reactants, and the second describes the partial charge transfer that occurs as the frontier orbitals of the electrophile and nucleophile interact. The contribution of each term to ( $\Delta E$ ) depends primarily on  $|E_{\text{HOMO}} - E_{\text{LUMO}}|$ . When this is large ( $|E_{\text{HOMO}} - E_{\text{LUMO}}| \gg 4\beta^2$ ), the Coulombic interaction dominates, and the reaction is charge controlled. If  $Q_{\text{nucleophile}}$  and  $Q_{\text{electrophile}}$  are both small and  $E_{\text{HOMO}}$  and  $E_{\text{LUMO}}$  are close in energy ( $|E_{\text{HOMO}} - E_{\text{LUMO}}| \approx 0$ ), then the second term in eq 5 dominates, and the reaction is orbitally controlled.

The DFT calculations on  $[(\text{NH}_3)_3\text{MoO}_2\text{X}]^+$  (X = Cl,  $\text{SCH}_3$ ,  $\text{OCH}_3$ ), before reaction, reveal estimated charges on the oxo

(78) Holm, R. H.; Kennepohl, P.; Solomon, E. I. *Chem. Rev.* **1996**, 96, 2239–2314.

(79) Xiao, Z.; Gable, R. W.; Wedd, A. G.; Young, C. G. *J. Am. Chem. Soc.* **1996**, 118, 2912–2921.

(80) Tucci, G. C.; Donahue, J. P.; Holm, R. H. *Inorg. Chem.* **1998**, 37, 1602–1608.

(81) Fleming, I. *Frontier Orbitals and Organic Chemical Reactions*; John Wiley & Sons: Chichester, 1976.



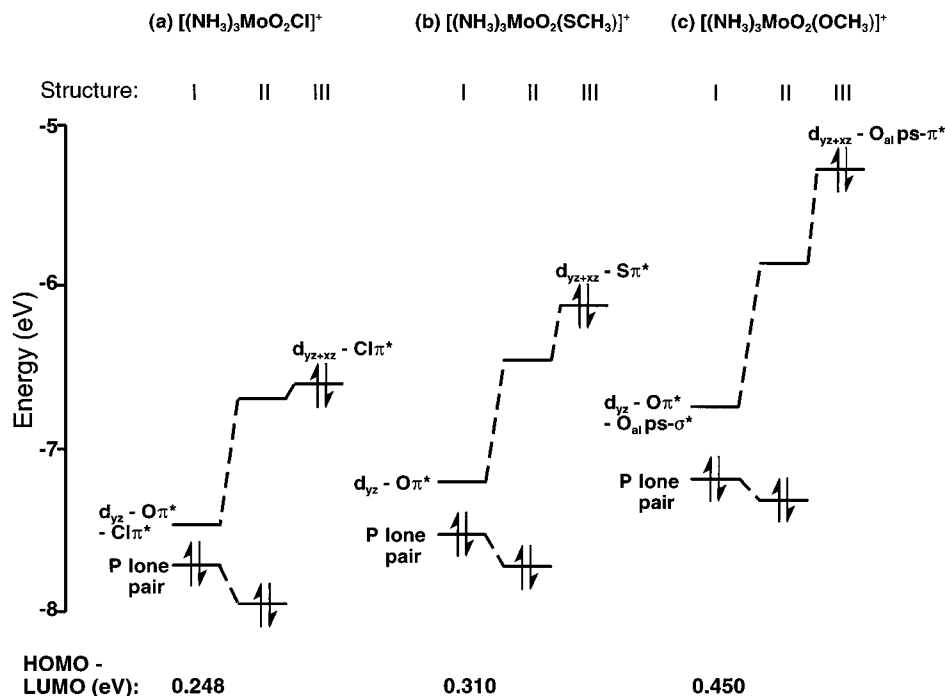


**Figure 9.** Energy change of the HOMO of  $P(CH_3)_3$  and the LUMO of  $[(NH_3)_3MoO_2X]^+$  ( $X = Cl, SCH_3, OCH_3$ ) over the OAT reaction coordinate. Structure **I** is before the reaction, **II** is with  $P-O = 2.43 \text{ \AA}$ , and **III** is with  $P-O = 1.53 \text{ \AA}$  (see Scheme 2).

groups of  $-0.53$  ( $X = Cl$ ),  $-0.57$  ( $X = SCH_3$ ), and  $-0.58$  ( $X = OCH_3$ ) and  $|E_{HOMO} - E_{LUMO}|$  values of  $0.248$  ( $X = Cl$ ),  $0.310$  ( $X = SCH_3$ ), and  $0.450$  ( $X = OCH_3$ ). Both trends predict a reactivity order  $Cl > SCH_3 > OCH_3$ , which parallels the reactivity order in Table 1. However, the small values of  $|E_{HOMO} - E_{LUMO}|$  and the larger variation of  $|E_{HOMO} - E_{LUMO}|$  relative to  $Q_{nucleophile}$  for  $X = Cl, SCH_3$ , and  $OCH_3$  indicate that OAT from  $[(NH_3)_3MoO_2X]^+$  to  $P(CH_3)_3$  is orbitally controlled and that  $|E_{HOMO} - E_{LUMO}|$  is the prime determinant of  $\Delta E$  across the series. The calculated values for  $c_{electrophile}^2$  (the total orbital character of the oxo group in the LUMO) are 25.84, 28.90, and 22.26% for  $X = Cl, X = SCH_3$ , and  $X = OCH_3$ , respectively, and do not follow the trend in reactivities. Presumably, this is related to the overestimation in calculated Mo 4d–Cl covalency (section 4B) that would tend to lower  $c_{electrophile}^2$  for  $X = Cl$ .

At structure **II**, the two electrons that will be donated to  $[(NH_3)_3MoO_2X]^+$  during OAT are still localized in a lone pair orbital on the P atom (HOMO of  $P(CH_3)_3$  molecule), and the Mo atom is in the formal VI oxidation state. As anticipated from eq 5, the additional HOMO stabilization at structure **II** is in the order  $X = Cl$  ( $0.247 \text{ eV}$ )  $>$   $X = SCH_3$  ( $0.208 \text{ eV}$ )  $>$   $X = OCH_3$  ( $0.117 \text{ eV}$ ) (Figure 9). Transfer of the two electrons from P to Mo gives geometry **III**, in which the  $d_{yz}$  and  $d_{xz}$  orbitals transform into a filled  $d_{yz+zx}$  orbital (directed toward  $O_1$ ) and an empty  $d_{yz-xz}$  orbital (directed toward  $O_2$ ). The  $Cl \pi^*$ ,  $S \pi^*$ , and  $O_{al} \pi^*$  contribute significantly to the  $d_{yz+zx}$  orbital (Figure 9). The relative energy of the HOMO ( $d_{yz+zx} - X \pi^*$ ) at structure **III** compared to that of the LUMO at structure **I** is in the order  $X = Cl$  ( $0.879$ )  $<$   $X = S$  ( $1.100$ )  $<$   $X = O_{al}$  ( $1.465 \text{ eV}$ ) (Figure 9). These values are in accord with the OAT reactivity order (Table 1); however, the approximations used to derive eq 5 may not remain valid when the reaction coordinate has progressed to structure **III**.

For  $X = SCH_3$  and  $OCH_3$  in structures **I**, **II**, and **III**, the  $C-S(O_{al})-Mo$  torsional angle (relative to the  $yz$ -plane) was held constant at  $0^\circ$  at all points along the reaction coordinate, as in the previous calculations.<sup>33</sup> The Walsh diagram in Figure 8 shows the dependence of the energies of the Mo  $d_{yz}$ (LUMO)

and  $d_{xz}$  orbitals, and the  $O_1$  and  $O_2 p_z$  character for the LUMO with torsional angle. For angles between  $0^\circ$  and  $180^\circ$ , there is a large variation in  $O_1$  and  $O_2 p_z$  character ( $0.1$ – $26.9\%$ ) and, consequently, in the antibonding character for each oxo group in the LUMO. Thus, in addition to LUMO energy modulation, the variation of the Mo–S–C torsional angle also serves as a mechanism for O atom selection. The oxo group with the greatest antibonding character in the LUMO will be transferred to  $PPh_3$  preferentially. For  $X = Cl$ , no such selection mechanism exists, and the oxo groups remain equivalent. This statistical effect may represent an additional factor in determining the rates of oxo atom transfer by  $LMoO_2X$  and the elevated reaction rate for  $X = Cl$ .

Besides anisotropic effects of the  $Cl, SCH_3$ , and  $OCH_3$  ligands and the energetic effects of the axial ligand on the O atom transfer reactivity,<sup>82</sup> steric factors may also play a role in the observed reactivity (Table 1). Both  $LMoO_2(SPh)$  and  $LMoO_2(OPh)$  are more sterically hindered than  $LMoO_2Cl$ , which reacts rapidly with  $PPh_3$ . However, the importance of electronic factors in reactivity, especially  $|E_{HOMO} - E_{LUMO}|$ , is supported by a comparison of the reactivities of  $LMoO_2(SPh)$  and  $LMoO_2(OPh)$ , which are of similar size. The  $SPh$  compound is 300 times more reactive, consistent with the DFT calculations and analyses presented above.

**C. Implications for Sulfite Oxidase.** Site-directed mutagenesis on human sulfite oxidase has shown that the coordination of a cysteine residue in addition to the ene-1,2-dithiolate derived from molybdopterin is essential for enzyme activity,<sup>18</sup> and  $S_{cys}$  coordination of the Mo center in the wild-type enzyme has been corroborated by the recent X-ray crystal structure of chicken liver sulfite oxidase (Scheme 1).<sup>9</sup> The differences between the Mo centers of the active wild-type and the inactive cysteine to serine mutant (C207S)<sup>18</sup> forms of human sulfite oxidase have been probed by EXAFS,<sup>14</sup> resonance Raman spectroscopy,<sup>17</sup> and S K-edge spectroscopy.<sup>14</sup> Particularly germane to the present work are the S K-edge difference spectra of the wild-type and

(82) Albright, T. A.; Burdett, J. K.; Whangbo, M. H. *Orbital Interactions in Chemistry*; John Wiley & Sons: New York, 1985.



the C207S mutant forms of oxidized human sulfite oxidase, showing a distinct pre-edge feature at 2468.0 eV.<sup>14</sup> Assuming that the covalency of the Mo–S bonds involving the ene-1,2-dithiolate is comparable for both the wild-type and mutant forms, the pre-edge feature in the difference spectrum is strong evidence for significant Mo–S<sub>cys</sub> covalency in the wild-type enzyme.<sup>14</sup>

The inactivity of the C207S mutant human enzyme shows that the coordinated cysteine residue, and presumably the covalency associated with its Mo–S bond, are essential for the biological function of sulfite oxidase.<sup>18</sup> Our analysis of the relative rates of reaction of LMo<sup>VI</sup>O<sub>2</sub>X (X = Cl, SPh, OCH<sub>3</sub>) with respect to OAT to PPh<sub>3</sub> has stressed the importance of the covalent anisotropic contributions of X in modulating the reduction potential and reactivity of [Mo<sup>VI</sup>O<sub>2</sub>X] cores. The X-ray crystal structure of sulfite oxidase shows a S<sub>cys</sub> donor cis to the O ligands (Scheme 1), permitting the full participation of the S lone pairs in determining the energy of the redox-active d<sub>yz</sub> or d<sub>xz</sub> orbital. This S<sub>cys</sub> ligation at the active site may determine the energy of the metal-based frontier orbital that is critical for determining the rate of sulfite oxidation by sulfite oxidase. The anisotropic covalency associated with the Mo–S<sub>cys</sub> bond may also serve as a switching mechanism during enzyme turnover to promote preferential transfer of one of the oxo groups (Figure 8). This idea is supported by the geometry at the active site of sulfite oxidase, where the methylene C atom of the cysteine residue is opposite the oxygen ligand that undergoes oxo transfer (the O=Mo–S–C dihedral angle = 179.1°); a similar geometry is observed for LMo<sup>IV</sup>O(pyridine)(SPh) (N<sub>pyridine</sub>–Mo–S–C = 161.2°). In addition, our rationalization of the relative Mo(VI)/Mo(V) reduction potentials of LMoO<sub>2</sub>X suggests that the S<sub>cys</sub> ligation may also fine-tune the Mo(VI)/Mo(V) reduction potential of the active site in sulfite oxidase that is essential in determining the rate of regeneration of the Mo(VI) active site during enzyme turnover (Scheme 1).

The ene-1,2-dithiolate ligation provided by molybdopterin should also be critical in determining the reduction potential and reactivity of the Mo center. This coordination has been implicated in enhancing the ability of the active site to catalyze OAT reactions by weakening the Mo=O bond through  $\pi$  electron donation to the metal,<sup>35</sup> by buffering the drastic changes in electron density at the Mo center that would be expected to accompany OAT,<sup>83</sup> and by providing a  $\sigma$ -electron-transfer pathway for regeneration of the active site during turnover.<sup>37</sup>

## 6. Summary

This study demonstrates for the first time that analyses of pre-edge X-ray absorption intensity can be extended to ligand S and Cl K-edge and Mo L-edge spectra of d<sup>0</sup> dioxo Mo<sup>VI</sup> complexes. A detailed electronic structure description of LMoO<sub>2</sub>X (X = Cl, SCH<sub>2</sub>Ph, OPh) has emerged from our spectroscopic results and DFT calculations on [(NH<sub>3</sub>)<sub>3</sub>MoO<sub>2</sub>X]<sup>+</sup> (X = Cl, SCH<sub>3</sub>, OCH<sub>3</sub>) analogues. The metal–ligand bonding is dominated by the two strong cis Mo=O bonds that control the splittings of the d orbitals, such that the LUMO is d<sub>yz</sub> in our coordinate frame (Figures 5 and 7). Covalent contributions from X, which perturb the energies of the d orbitals within the ligand field manifold, are superimposed on this orbital scheme (Figure 7). The principal perturbations due to X are Cl  $\pi^*$  to d<sub>yz</sub> and Cl  $\sigma^*$  to d<sub>xz</sub> for X = Cl, S  $\pi^*$  to d<sub>xz</sub>, and S pseudo- $\sigma^*$

to d<sub>xz</sub> for X = SCH<sub>3</sub>, and O<sub>al</sub> pseudo- $\sigma^*$  to d<sub>yz</sub> and O<sub>al</sub>  $\pi^*$  to d<sub>xz</sub> for X = OCH<sub>3</sub>. The theoretical orbital splittings and key covalent interactions due to X are directly reflected in the dominant experimental peak splitting and intensity variations within the Cl and S K-edge (Figures 2 and 3) and the Mo L<sub>2</sub>-edge spectra (Figure 4) for the complexes. However, the quantitative analysis of the Cl and S K-pre-edges reveals that the DFT calculations strongly overestimate Cl covalency, whereas there is a small underestimation of S covalency.

Anisotropic covalent interactions with X modulate the energy of the redox-active d<sub>yz</sub> orbital and thereby influence the relative Mo(VI)/Mo(V) reduction potentials and the relative rates of reaction of LMoO<sub>2</sub>X with PPh<sub>3</sub> (Table 1). The donor properties of X affect the LUMO (d<sub>yz</sub>)–HOMO (PPh<sub>3</sub> lone pair) energy gap, the charge on the oxo groups, and provide a mechanism for “oxygen atom selection”. The principal factors in determining the anisotropy of the covalent contributions of X to Mo are the O=Mo–S(O)–C dihedral and O=Mo–S(O) bond angles of the thiolate and alkoxide ligands. These angles restrict one of the ligand valence  $\pi$  orbitals from interacting with Mo and control the bonding participation of the remaining ligand valence orbitals within the metal d manifold.

Comparisons of sulfite oxidase with LMo<sup>VI</sup>O<sub>2</sub>X suggest that the S<sub>cys</sub> ligation at the active site of sulfite oxidase may be playing a similar role in determining the reactivity of the [Mo<sup>VI</sup>O<sub>2</sub>]<sup>2+</sup> center. The anisotropic covalency associated with the S<sub>cys</sub>–Mo bond may facilitate OAT through a modulation of the energies of the Mo 4d orbitals and the preferential selection of the O atom to be transferred during enzyme turnover. However, a more complete understanding of the role of cysteinyl ligation at the active site of sulfite oxidase must await a better definition of the role(s) of the novel ene-1,2-dithiolate coordination that is common to the active sites of all oxomolybdoenzymes. This study has demonstrated that the combined analyses of the S and Cl K pre-edge and the Mo L-edge XAS can provide details of the bonding framework of LMo<sup>VI</sup>O<sub>2</sub>X complexes, a basis for understanding their chemical properties, and insights into the role of S<sub>cys</sub> ligation at the active site of sulfite oxidase.

**Acknowledgment.** This work was supported by grants from NSF (CHE-9528250, E.I.S., and CHE-9423181, K.O.H.) and NIH (GM-37773, J.H.E and RR-01209, K.O.H.). SSRL operations are funded by the Department of Energy, Office of Basic Energy Sciences. The Biotechnology Program is supported by the National Institutes of Health, National Center for Research Resources, Biomedical Technology Program. Further support is provided by the DOE, Office of Biological and Environmental Research. Y.I. was supported at Stanford University by a Foreign Research Scientist Fellowship funded by the Ministry of Education, Science, Sports, and Culture (Monbusho) of Japan. T.G. thanks the Deutsche Forschungsgemeinschaft for a post-doctoral fellowship. We thank Dr. C. G. Young for advice on the synthesis of the Mo complexes.

**Supporting Information Available:** Peak fits and spectral assignments for the Mo L<sub>2</sub>-edge data, and tables of detailed geometric parameters for the MO calculations and the energy splittings within the L<sub>3</sub>-edge spectra of LMoO<sub>2</sub>(SCH<sub>2</sub>Ph), LMoO<sub>2</sub>Cl, and LMoO<sub>2</sub>(OPh) (PDF). This material is available free of charge via the Internet at <http://pubs.acs.org>.

(83) Westcott, B. L.; Gruhn, N. E.; Enemark, J. H. *J. Am. Chem. Soc.* **1998**, *120*, 3382–3386.